Mitochondrial fission process 1 (MTFP1) controls bioenergetic efficiency and prevents inflammatory cardiomyopathy and heart failure in mice

Erminia DONNARUMMA[1], Michael KOHLHAAS[2], Elodie VIMONT[1], Etienne KORNOBIS[3, 4], Thibault CHAZE[5], Quentin GIAI GIANETTO[4,5], Mariette MATONDO[4], Maryse MOYA-NILGES[5], Christoph MAACK[2], Timothy WAI[1,*]

1-Institut Pasteur, Mitochondrial Biology Group, CNRS UMR 3691, Paris, France

2-Department of Translational Research, Comprehensive Heart Failure Center (CHFC), University Clinic Würzburg, Würzburg, Germany

3- Plate-forme Technologique Biomics – Centre de Ressources et Recherches Technologiques (C2RT), Institut Pasteur, Paris, France

4- Hub de Bioinformatique et Biostatistique - Département Biologie Computationnelle, Institut Pasteur, 75015 Paris, France

5- Institut Pasteur, Proteomics Platform, Mass Spectrometry for Biology Unit, USR CNRS 2000, Paris, France

6-Institut Pasteur, UTechS Ultrastructural Bio Imaging, Paris, France

*Correspondence: timothy.wai@pasteur.fr

Keywords: mitochondria, cardiomyopathy, oxidative phosphorylation, uncoupling, permeability transition pore

28 ***Abstract***

29 Mitochondria are paramount to the metabolism and survival of cardiomyocytes. Here we show that

30 Mitochondrial Fission Process 1 (MTFP1) is essential for cardiac structure and function.

31 Constitutive knockout of cardiomyocyte MTFP1 in mice resulted in adult-onset dilated

32 cardiomyopathy (DCM) characterized by sterile inflammation and cardiac fibrosis that progressed

33 to heart failure and middle-aged death. Failing hearts from cardiomyocyte-restricted knockout

34 mice displayed a general decline in mitochondrial gene expression and oxidative phosphorylation

35 (OXPHOS) activity. Pre-DCM, we observed no defects in mitochondrial morphology, content, gene

36 expression, OXPHOS assembly nor phosphorylation dependent respiration. However, knockout

37 cardiac mitochondria displayed reduced membrane potential and increased non-phosphorylation

38 dependent respiration, which could be rescued by pharmacological inhibition of the adenine

39 nucleotide translocase ANT. Primary cardiomyocytes from pre-symptomatic knockout mice

40 exhibited normal excitation-contraction coupling but increased sensitivity to programmed cell death

41 (PCD), which was accompanied by an opening of the mitochondrial permeability transition pore

42 (mPTP). Intriguingly, mouse embryonic fibroblasts deleted for *Mtfp1* recapitulated PCD sensitivity

43 and mPTP opening, both of which could be rescued by pharmacological or genetic inhibition of the

44 mPTP regulator Cyclophilin D. Collectively, our data demonstrate that contrary to previous in vitro

45 studies, the loss of the MTFP1 promotes mitochondrial uncoupling and increases cell death

46 sensitivity, causally mediating pathogenic cardiac remodeling.

47

48

49   **_Introduction_**

50   Mitochondria are multifaceted organelles that are essential in every tissue of the body and are

51   most abundant in the heart, where they control the metabolism and survival of cardiac cells

52   (Kolwicz et al., 2013). Mitochondria are double membrane-bound organelles, composed of an

53   inner (IMM) and an outer mitochondrial membrane (OMM), which separate the intermembrane

54   space (IMS) from the matrix. The IMM extends internally to form cristae, which harbor essential

55   macromolecular complexes such as the machinery of oxidative phosphorylation (OXPHOS). The

56   OXPHOS system is comprised of two functional entities: the electron transport chain (ETC) and

57   the phosphorylation system, which includes the integral membrane ATP synthase and carriers

58   such as the adenine nucleotide translocase (ANT), which imports ADP into the matrix and exports

59   ATP (Chance and Williams, 1956). The ETC is composed of four macromolecular complexes (I, II,

60   III, and IV) and of mobile electrons carriers as coenzyme Q (CoQ) and cytochrome-c (Cyt *c*). The

61   energy available for ATP synthesis is directly derived from the membrane potential (ΔΨ) and

62   proton motive force generated across the IMM by electron transfer from by the ETC, which is then

63   harnessed by the ATP synthase (complex V) to generate ATP (Mitchell, 1961). Continuous

64   generation of ATP is fundamental for the function of cardiomyocytes, enabling them to meet the

65   enormous energy requirement for the contraction–relaxation cycles that drive their contractility

66   (Kohlhaas et al., 2017). Defects that impair OXPHOS assembly and function can promote fatal

67   cardiomyopathies (Antonicka et al., 2003a, 2003b; Graham et al., 1997; Hansson et al., 2004;

68   Karamanlidis et al., 2013). The beating heart demands near-maximum OXPHOS capacity, with

69   scant aerobic ATP reserves under normal conditions (Mootha et al., 1997). Consequently, even

70   modest uncoupling of the ETC from ATP synthesis, which can occur when protons are diverted

71   back across the IMM through uncoupling channels rather than being used by the ATP synthase,

72   would be expected to yield fatal consequences for cardiac function and health, although this has

73   never been tested.

74   While most famous for their role as the powerhouse of the cell, mitochondria have proven to be

75   essential for cardiac homeostasis through the regulation of various biosynthetic and signaling

76   functions beyond OXPHOS, such as calcium buffering, reactive oxygen species (ROS) generation

77   and maintenance, programmed cell death (PCD) and innate immune responses (Zhou and Tian,

78   2018). Under stress conditions, extrinsic or intrinsic signals can lead to a permeabilization of the

3

79   outer membrane (MOMP) resulting in activation of caspases and PCD (Bock and Tait, 2020). At

80   the IMM, long-lasting opening of the mitochondrial permeability transition pore (mPTP) allows for

81   unselective diffusion of low molecular weight solutes and water (<1.5 kDa), causing an osmotic

82   pressure in the matrix that causes mitochondrial swelling (Carraro et al., 2020) and rupture,

83   thereby releasing pro-apoptotic and pro-inflammatory mitochondrial factors into the cytosol (Bock

84   and Tait, 2020). While the molecular identity of the mPTP is still the subject of feverous debate, to

85   date several factors have been identified to be unequivocally crucial for its activation. Cyclophilin D

86   (CypD, encoded by *Ppif*), a mitochondrial matrix isomerase which can be inhibited

87   pharmacologically by cyclosporin A (CsA), calcium overload and ROS are known to promote

88   mPTP opening and PCD induction (Baines et al., 2005; Carraro et al., 2020; Nakagawa et al.,

89   2005). Notably, ablation of CypD or treatment with CsA can protect animals from cardiomyocyte

90   death and cardiomyopathy induced by genetic (Song et al., 2015), infectious (Milduberger et al.,

91   2021), and surgical lesions (Nakagawa et al., 2005).

92   The maintenance of mitochondrial morphology and structure is of critical importance for

93   cardiac function (Sprenger and Langer, 2019). Mitochondrial morphology is regulated by opposing

94   forces of mitochondrial fusion and division, which must be tightly regulated to ensure organellar

95   function and quality control (Giacomello et al., 2020; Ng et al., 2021). Intrinsic (Ashrafian et al.,

96   2010; Chen et al., 2015; Kageyama et al., 2014; Song et al., 2015; Wai et al., 2015) or extrinsic

97   (Acin-Perez et al., 2018; Chen et al., 2009; Shirakabe et al., 2016) lesions that upset the balance

98   between mitochondrial fission and fusion have devastating consequences for cardiomyocyte

99   function and cardiac health. Mitochondrial dynamics is orchestrated by dynamin-like GTPases:

100   OPA1 and mitofusins (MFN1/2) execute inner and outer membrane fusion, respectively, while

101   DRP1 performs mitochondrial constriction and division once recruited to the OMM via interactions

102   that require integral membrane proteins and receptors, such as MFF, MiD49/51, and FIS1. DRP1

103   is the lynchpin of the mitochondrial fission apparatus, which is triggered to coalesce at contact

104   sites with the ER, lysosomes, trans-golgi network, and actin by signals that can originate both

105   outside (Cretin et al., 2021; Giacomello et al., 2020) and inside (Cho et al., 2017; Lewis et al.,

106   2016; Tondera, 2005) mitochondria.

107   While it is unclear how IMM fission is executed, the aptly-named inner membrane protein

108   Mitochondrial fission process 1 (MTFP1/MTP18), has emerged as a promising scaffold for the IMM

109   division apparatus, whose formal identification remains elusive (Ng et al., 2021). As per its

110   namesake, *Mtfp1* was initially identified as a gene whose ablation was reported to reduce

111   mitochondrial fission, as well as the proliferation and viability of cultured cells (Tondera, 2005;

112   Tondera et al., 2004). The pro-apoptotic effects of *Mtfp1* depletion have been replicated in various

113   cell lines (Duroux-Richard et al., 2016; Wang et al., 2017), however, more recent studies by the Li

114   group (Aung et al., 2017a, 2017b; Wang et al., 2017) have reported the contrary in cultured cells,

115   thus fueling the existing narrative that elongated mitochondria resulting from MTFP1 depletion

116   protects cells from PCD. Whether this paradigm holds true in vivo has never been explored.

117   In this study, we created a cardiomyocyte-specific *Mtfp1* knockout mouse model to

118   specifically investigate the role of this protein in vivo. Contrary to previous in vitro studies (Wang et

119   al., 2017), we show that MTFP1 plays an essential role in maintaining cardiac energy metabolism

120   as its deletion in post-natal cardiomyocytes drives a progressive dilated cardiomyopathy (DCM)

121   culminating in HF and middle-aged death in mice. Surprisingly, MTFP1 ablation does not

122   appreciably alter mitochondrial morphology in the heart and is entirely dispensable for

123   mitochondrial fission. Unexpectedly, we discovered that MTFP1 depletion reduces OXPHOS

124   efficiency in cardiac mitochondria by increasing proton leak through the adenine nucleotide

125   translocase (ANT). Finally, we show MTFP1 ablation increases mPTP opening and renders

126   cardiomyocytes and embryonic fibroblasts more sensitive to PCD. Altogether, our data reveal an

127   unexpected role of MTFP1 in mitochondrial bioenergetics and provide mechanistic insights into

128   how MTFP1 regulates the life and death of the cell.

129

Results

Mtfp1 deletion in cardiomyocytes causes dilated cardiomyopathy and middle-aged death

MTFP1 is predicted to localize in mitochondrial inner membrane (Figure 1A), and *MTFP1* is highly expressed in human cardiac tissue (GTEx plot, Figure S1A). To investigate the importance of MTFP1 for cardiac function we began by confirming its expression and submitochondrial localization in the mouse heart. Protease protection assays and alkaline carbonate extraction experiments performed on isolated cardiac mitochondria allowed us to demonstrate the inner membrane localization of MTFP1 in cardiac mitochondria (Figure S1B-C). To investigate its role in vivo, we generated a conditional mouse model for *Mtfp1* (*Mtfp1^LoxP/LoxP^*) on a C57Bl6/N background. Conditional mice were crossed with transgenic mice expressing Cre recombinase under the control of alpha myosin heavy chain promoter (Agah et al., 1997) (Myh6) to specifically ablate MTFP1 in post-natal cardiomyocytes (Figure 1B, S1D). We previously showed that genetic deletion mediated by Myh6-Cre occurs during the perinatal period (Wai et al., 2015) and by 8 weeks of age cardiomyocyte-specific *Mtfp1* KO mice (Myh6-Cre^Tg/+^ *Mtfp1 ^LoxP/LoxP^*, cMKO mice) exhibited a 7-fold reduction in *Mtfp1* mRNA (Figure 1C) and undetectable levels of MTFP1 protein in cardiac lysates assessed by immunoblot analysis (Figure 1D) and shotgun proteomics (Figure 1E, Dataset EV1). Both male and female cMKO mice were generated according to Mendelian proportions and were outwardly normal and viable. However, cMKO mice had significantly shortened lifespans [median life span: 26.4 weeks (male), 37.5 weeks (female)] relative to wild type (WT) littermates (Figure 1F, Figure S1E), demonstrating that MTFP1 is required to protect against middle-aged death.

To directly assess the importance of MTFP1 for cardiac structure and function, we performed longitudinal echocardiographic (echo) studies in male and female mice (Figure 1G-L, S1F-K). Echo analyses beginning at 10 weeks of age revealed normal cardiac structure and function in cMKO mice. By 18 weeks, however, despite normal cardiac structure we observed a progressive decrease in systolic function, culminating in dilated cardiomyopathy (DCM) and left ventricle (LV) remodeling. By 34 weeks, cMKO mice exhibited all the hallmarks of DCM and heart failure (HF): significantly reduced LV ejection fraction [% EF, WT 60.31 ± 5.4 % *versus* cMKO 25.87 ± 11.8 %; Figure 1H] , thinning of the interventricular septum in systole [IVS (mm), WT 1.23 ± 0.097 *versus* cMKO 0.9 ± 0.092; Figure 1I], posterior wall during systole [PWs (mm), WT $1.39 \pm$

6

160   0.10 *versus* cMKO 0.952 ± 0.17; Figure 1J), dilated LV chamber during the cardiac cycle of

161   diastole [LVDD (mm), WT 4.00 ±0.15 *versus* cMKO 5.02 ± 0.65, Figure 1K] and systole [LVSD

162   (mm), WT 2.72 ± 0.16 *versus* cMKO 4.43 ± 0.84; Figure 1L) with pulmonary congestion (Figure

163   S1L) and increased heart mass at severe HF (Figure S1M).

164   To determine whether the progressive cardiac contractile dysfunction observed in cMKO

165   mice was caused by primary defects in cardiomyocyte function, we assessed sarcomere length

166   and shortening (Figure S1N-P) coupled to intracellular Ca^{2+} levels $[Ca^{2+}]_c$ (Figure S1Q-S) in field-

167   stimulated cMKO cardiomyocytes isolated from pre-symptomatic mice (8-10 weeks of age).

168   Diastolic and systolic sarcomere length as well as $[Ca^{2+}]_c$ transients were similar between WT and

169   cMKO myocytes both at baseline (0.5 Hz stimulation frequency) and during β-adrenergic

170   stimulation (5 Hz stimulation frequency) despite a modest increase of sarcomere shortening of

171   cMKO myocytes under stress conditions and a normal sarcomere re-lengthening at baseline

172   conditions. Together, these data indicate that *Mtfp1* deletion does not impinge upon cardiomyocyte

173   excitation-contraction coupling before the onset of cardiomyopathy in vivo.

174   Histological analyses of cMKO hearts of mice at HF (34 weeks) confirmed defects in

175   cardiac structure: hematoxylin-eosin (H&E) staining of cardiac cross sections showed LV chamber

176   expansion and myocardial wall thinning, while Masson's trichrome and Picrosirius Red staining

177   showed disruption of the myofibril architecture by dramatic fibrosis and collagen deposition at DCM

178   (Figure 1M). We also found increased serum levels of cardiac troponin I (cTNI, Figure 1N) and

179   myosin light chain 1 (MLC-1, Figure 1O) in cMKO mice sampled at 18 and 34 weeks, further

180   substantiating the ongoing cardiomyocyte damage and death. We did not observe gender

181   differences in the development of the cardiac dysfunction (Figure S1F-K), highlighting the essential

182   nature of MTFP1 for cardiac structure and function.

183

184   **Metabolic and inflammatory gene expression dysregulation in cMKO mice**

185   To gain further insights into the molecular and cellular mechanisms underlying cardiac pathology in

186   cMKO mice, we performed transcriptomic analyses by bulk RNA sequencing (RNAseq) of LVs

187   isolated from WT and cMKO mice at a pre-symptomatic stage (8 weeks of age) and at the onset of

188   DCM (18 weeks). We observed up-regulation of *Nppa* in pre-symptomatic cMKO mice, which was

189   associated to up-regulation of *Nppb* at the onset of DCM, prototypical cardiomyocyte stress-

190 response genes that are activated in response to hemodynamic load (Hohl et al., 2013) and

191 metabolic or contractile abnormalities (Houweling et al., 2005) (Figure 1P). At the pre-symptomatic

192 stage, we observed limited transcriptional remodeling in hearts from cMKO mice with differential

193 expression of only ~1% of 25815 genes: 137 genes were downregulated, and 122 genes were

194 upregulated in cMKO mice (Dataset EV2, Figure 1P), whereas at 18 weeks, we observed a much

195 broader transcriptional response with 3642 differentially expressed genes in cMKO mice

196 manifesting early signs of DCM (Dataset EV2, Figure 1P).

197 Functional enrichment analyses performed with g:Profiler (Reimand et al., 2019) and

198 Enrichr (Chen et al., 2013) revealed a number of dysregulated genes involved in various metabolic

199 processes (Figure 1Q, left). Among the downregulated genes with the gene ontology (GO) term

200 metabolic process (Dataset EV2) were genes required for OXPHOS, TCA cycle, fatty acid

201 oxidation and pyruvate metabolism, suggestive of cardiometabolic changes previously observed in

202 mitochondrial models of HF (Hansson et al., 2004; Liao et al., 2015; Wai et al., 2015; Zhou and

203 Tian, 2018). In fact, further examination revealed that half of all mitochondrial genes referenced on

204 MitoCarta (Rath et al., 2021) were downregulated (Figure 1Q, middle). On the other hand, we

205 observed a strong sterile inflammatory gene expression signature and innate immune engagement

206 (Figure 1Q, right), which together with dysregulated extracellular matrix-remodeling genes

207 [profibrotic cytokines such as TGFb, collagen precursor genes (*Col11a1, Col14a1, Col8a1*) and

208 matrix metalloproteinases (*Mmp-2, Mmp-14, Mmp-3*)] (Figure 1R) corroborates the cardiac fibrosis

209 revealed by histological analysis of cMKO hearts (Figure 1M). Notably, the suppression of

210 mitochondrial gene expression and the activation of sterile inflammation measured in cMKO mice

211 at 18 weeks was absent in pre-symptomatic cMKO mice, implying that these transcriptional

212 responses are downstream consequences *Mtfp1* deletion in adult cardiomyocytes.

213

214 ***Mtfp1 is required for bioenergetic efficiency in cardiac mitochondria***

215 To directly assess the effects of energy metabolism in cMKO mice, we measured mitochondrial

216 respiration in cardiac mitochondria from WT and cMKO mice (Figure 2A). High resolution

217 respirometry studies showed a general impairment of mitochondrial O_2 consumption in cMKO

218 hearts at both early and late stage of DCM: complex I-, complex II- and complex IV-driven

219 mitochondrial respiration were all significantly lower at either age (Figure 2B, C). Interestingly,

8

reduced mitochondrial respiration was not accompanied by reduced levels of mitochondrial proteins, including those involved in OXPHOS (Figure S2A-B, Dataset EV1), demonstrating that bioenergetic decline was not the result of increased wholesale mitophagy.

Since reduced mitochondrial content and/or OXPHOS activity has been observed in other genetic models of cardiomyopathy (Burke et al., 2016), we wondered whether impaired mitochondrial respiration observed in failing cMKO hearts reflected the consequences of cardiac dysfunction and cardiac remodeling, rather than the ablation of an essential component or regulator of OXPHOS. We observed no deficits of the mitochondrial Krebs cycle in intact field-stimulated cMKO cardiomyocytes assessed by determining the autofluorescence of $NAD(P)H/NAD(P)^+$ and $FADH_2/FAD$, intrinsic biomarkers of mitochondrial metabolic activity. NAD(P)H/FAD redox state was monitored during a protocol in which cells were exposed to an increase in stimulation frequency and β-adrenergic stimulation(Bertero et al.), creating a typical ADP-induced oxidation ("undershoot") followed by Ca^{2+}-dependent regeneration ("recovery") behavior (Cortassa et al., 2003)(Figure S2C). This behavior was similar between cMKO and WT myocytes (Figure S2C), ruling out gross alterations in Krebs cycle activity and Ca^{2+}-induced redox adaptation.

To uncover the functional alterations of OXPHOS that potentiate the development of DCM, we performed bioenergetic measurements in cardiac mitochondria isolated from pre-symptomatic mice. Using a dual respirometer-fluorimeter (O2k, Oroboros), simultaneous kinetic measurements of oxygen consumption rates (JO_2) and mitochondrial membrane potential ($\Delta\Psi$) were performed in cardiac mitochondria isolated from pre-symptomatic WT and cMKO mice (8-10 weeks). Active mitochondria were pre-labeled with the potentiometric dye Rhodamine-123 (RH-123) and energized with substrates whose metabolism promotes complex I- [state 2; pyruvate, glutamate, and malate (PGM)] or complex II-linked respiration (state 2; succinate and rotenone), followed by ADP to promote phosphorylating (state 3: ADP) respiration. Finally, the ATP synthase inhibitor oligomycin (Omy) was applied to assess non-phosphorylating (state 4) respiration (Figure 2A).

We observed no differences in state 3 JO_2 rates between WT and cMKO cardiac mitochondria fueled with either PGM, succinate with rotenone or palmitoyl-carnitine with malate, respectively (Figure 2D (left), Figure S2D (left), F). However, respiration was ~30% higher in cMKO mitochondria in state 2 (+27.4 %) and state 4 (+30.3 %) when complex I was fueled with PGM

9

250 (Figure 2D), significantly decreasing respiratory control ratios [State 3:2, State 3:4, Figure 2D

251 (middle, right)]. In addition, altered JO_2 rates in cMKO mitochondria were accompanied by

252 impaired RH-123 quenching in state 2 and state 4 (Figure 2E, S2E), indicating defective IMM

253 substrate-dependent hyperpolarization. Supporting the notion that MTFP1 ablation increases

254 proton leak, we consistently observed reduced respiratory control ratios when complex II was

255 energized (Figure S2D, middle-right) and lower mitochondrial membrane potential under both state

256 2 and state 4 conditions regardless of the respiratory substrates that were provided (Figure S2D-

257 E).

258 The elevated JO_2 rates and reduced RH-123 quenching in state 4 could be explained either

259 by a reduced sensitivity of the ATP synthase to Omy treatment or by uncoupling caused by proton

260 leak across the IMM. In the mouse heart, reduced Omy sensitivity can result from defects in the

261 assembly of the ATP synthase that alter the affinity of Omy binding to Complex V via OSCP

262 (Mourier et al., 2014). However, BN-PAGE analyses of cardiac mitochondria isolated from pre-

263 symptomatic cMKO mice revealed no defects in ATP synthase assembly/maintenance (Figure 2F),

264 leaving us with increased proton leak as the most parsimonious explanation for the observed state

265 4 respiration and membrane potential differences (Figure 2D, E; Figure S2D-E).

266 Next, we sought to corroborate our findings in cultured cells. To this end, we generated MTFP1-

267 deficient mouse embryonic fibroblasts (MEFs) (*Mtfp1*$^{-/-}$) and MTFP1-deficient human U2OS cells

268 by Crispr/Cas9 genome editing (*MTFP1*^{Crispr}) and corresponding WT (*MTFP1*$^{+/+}$) controls (Figure

269 S2H, I) and then assessed oxygen consumption by Seahorse FluxAnalyzer. Intriguingly, we

270 observed no changes in basal or maximal respiration rates nor any evidence of mitochondrial

271 uncoupling (Figure S2J-Q) suggesting that MTFP1-dependent proton leak may be cell type

272 specific.

273 Taken together, our data reveal an unappreciated and critical role of MTFP1 in bioenergetic

274 efficiency and mitochondrial uncoupling, particularly evident in metabolically active

275 cardiomyocytes, which precedes the manifestation of cardiac dysfunction and heart failure in

276 cMKO mice.

277

278 ***Mitochondrial uncoupling is mediated by the Adenine Nucleotide Translocase***

10

279 To uncover the mechanism responsible for the mild mitochondrial uncoupling caused by *Mtfp1*

280 deletion in cardiomyocytes, we turned our attention to known uncoupling proteins. Uncoupling

281 proteins (UCPs, UCP 1/2/3) and adenine nucleotide translocase (ANT) IMM proteins have been

282 reported to be the two main catalysts of futile proton leak in mammalian mitochondria (Brand et al.,

283 2004; Echtay et al., 2002). UCP1 is a bona fide uncoupler that is primarily expressed in brown

284 adipose tissue (Adams, 2000) and shares significant sequence similarity with UCP2 and 3, which

285 are expressed in other tissues (Woyda-Ploszczyca and Jarmuszkiewicz, 2014). ANT is an integral

286 IMM transporter that imports ADP and concomitantly exports ATP between the mitochondrial

287 matrix and IMS (Ruprecht and Kunji, 2021). ANT exists in four different tissue specific isoforms

288 (ANT1, 2, 3, and 4), with ANT1 being the most abundant protein in mitochondria (Lu YW et al,

289 2017, Brand MD et al, 2005; Karch et al., 2019; JE Kokoszka et al., 2016). ANT1 has long been

290 known for its namesake role as a nucleotide translocator, and recent studies have proven it to be

291 an essential transporter of protons across the IMM in mammals (Bertholet et al., 2019) and a rate-

292 liming factor for proton leak in *Drosophila* (Brand et al., 2005). While the steady state levels of

293 ANT in cardiac tissue of WT and cMKO mice were identical (Figure 2G), we nevertheless sought to

294 functionally assess the contribution of ANT to MTFP1-dependent proton leak in freshly isolated

295 cardiac mitochondria by using the ANT antagonist carboxyatractyloside (CATR), which binds

296 irreversibly to ANT on the IMS side of the IMM, blocking its activity (Todisco et al., 2016). The

297 addition of CATR alone or after Omy treatment rescued the reduced $\Delta\Psi$ and elevated JO_2 rates

298 back to WT levels (Figure 2H-I), normalizing the respiratory control ratio for state 3:4 (Figure 2J),

299 suggesting that *Mtfp1* deletion increases ANT-dependent proton leak.

300   To exclude the unlikely possibility that other uncoupling proteins such as UCPs might

301 contribute to increased proton leak caused by *Mtfp1* ablation, we measured $\Delta\Psi$ of cardiac

302 mitochondria in the presence of GTP, a pyrimidine nucleotide previously demonstrated to potently

303 inhibit uncoupling in vitro (Macher et al., 2018; Woyda-Ploszczyca and Jarmuszkiewicz, 2014).

304 UCP inhibition with GTP was not able to rescue the defective membrane potential observed in

305 Omy-treated cMKO mitochondria (Figure 2K) suggesting that UCPs do not contribute to the futile

306 proton leak in cMKO cardiac mitochondria. Taken together, these data demonstrate that depletion

307 of MTFP1 in the IMM leads to an increased uncoupling activity of ANT, resulting in proton leak and

308 bioenergetic inefficiency preceding the development of cardiac dysfunction (Figure S2R).

11

309

MTFP1 is dispensable for mitochondrial fission.

310

311 Transient MTFP1 knock-down has previously been reported to promote mitochondrial elongation in

312 a variety of cultured cell types including neonatal cardiomyocytes (Duroux-Richard et al., 2016;

313 Morita and Terada, 2015; Tondera et al., 2009; Wang et al., 2017), yet the consequence in the

314 adult heart has never been explored. Therefore, to determine the impact of *Mtfp1* deletion on

315 mitochondrial morphology, we co-labeled primary WT and cMKO primary adult cardiomyocytes

316 (CMs) with tetramethylrhodamine ethyl ester (TMRE) and Mitotracker Deep Red (MTDR) to

317 visualize mitochondria. Contrary to previous reports purporting that *Mtfp1* depletion causes

318 mitochondrial elongation (Aung et al., 2017a, 2019), we failed to observe any obvious effects on

319 the morphology, distribution, or content of mitochondria in primary adult CMs deleted of *Mtfp1*

320 (Figure 3A-B). Similarly, transmission electron microscopy (TEM) analyses of pre-symptomatic

321 cMKO and WT hearts (LV) showed no indications of mitochondrial elongation (median

322 mitochondrial surface area: WT 3198 μm^2 versus cMKO 2954 μm^2) nor altered cristae organization

323 (Figure 3C-D). We also did not observe changes in mtDNA content (Figure 3E) or mitochondrial

324 shaping proteins in cardiac biopsies: the steady-state levels of fusion (MFN1, MFN2, OPA1) and

325 fission (DRP1, MID51, FIS1) proteins were no different between WT and cMKO mice (Figure 3F).

326 Thus, MTFP1 is dispensable for mitochondrial dynamics in the heart.

327 In light of these surprising findings, we decided to measure mitochondrial morphology in MEFs

328 depleted of MTFP1 under basal and stress conditions using a recent supervised machine learning

329 (ML) approach we developed for high-throughput image acquisition and analyses (Cretin et al.,

330 2021). In contrast to previous reports, MEFs depleted (siRNA *Mtfp1*) or deleted (*Mtfp1$^{-/-}$*) of *Mtfp1*

331 showed only modest elongation of the mitochondrial network: both transient (siRNA) or chronic

332 (knockout) ablation of MTFP1 resulted in ~15% increase in hypertubular mitochondria (Figure 3I-

333 J), and *Mtfp1$^{-/-}$* MEFs showed unaltered steady-state levels of mitochondrial fusion and fission

334 proteins (Figure S3A). Contrary to DRP1-deficient cells (Cretin et al., 2021), *Mtfp1$^{-/-}$* MEFs were

335 not protected from mitochondrial fragmentation induced by established pharmacological triggers of

336 mitochondrial fragmentation, such as oligomycin (Omy), Rotenone, hydrogen peroxide (H_2O_2), or

337 carbonyl cyanide m-chlorophenylhydrazone (CCCP) (Figure 3G-H). Similarly, *Mtfp1$^{-/-}$* MEFs were

338 not protected from genetic induction of mitochondrial fragmentation by depletion of *Yme1l* or *Opa1*

12

339   (Figure 3I-J). While we could confirm that MTFP1 overexpression is able to promote mitochondrial

340   fragmentation in MEFs, without affecting steady state level of fusion and fission proteins (Figure

341   S3B-C), our data collectively indicate that MTFP1, unlike DRP1, is not an essential fission protein.

342   Taken together, these results strongly argue that contrary to its namesake, MTFP1 is not an

343   essential fission factor either in vitro or in vivo.

344

345   ***MTFP1 deletion promotes mitochondrial permeability transition pore opening and***

346   ***programmed cell death.***

347   Cardiomyocyte death is catastrophic for adult cardiac function because of the limited regenerative

348   capacity of these post-mitotic cells. Given the appearance of cardiac cell damage and death in

349   cMKO mice during DCM (Figure 1N-O), we sought investigate whether MTFP1 loss specifically

350   increased cell death sensitivity. To this end, we isolated adult primary cardiac myocytes (CMs)

351   from WT and pre-symptomatic cMKO mice between 8-10 weeks of age and kinetically measured

352   cell survival in response to a variety of cell death triggers using supervised ML-assisted high-

353   throughput live-cell imaging (Cretin et al., 2021). We were able to isolate equally viable CMs from

354   both WT and cMKO mice, yet upon dissipation of the membrane potential with CCCP (Figure 4A-

355   B) or treatment with H_2O_2 (Figure 4C-D), $Mtfp1^{-/-}$ CMs succumbed to cell death more rapidly than

356   WT CMs. Moreover, the induction of cell death with doxorubicin (DOXO, Figure 4E-F), a

357   cardiotoxic chemotherapeutic agent that triggers programmed cell death (PCD) (Christidi and

358   Brunham, 2021), induced a significant increase of death in $Mtfp1^{-/-}$ compared to WT CMs,

359   indicating that MTFP1 is essential for cell survival.

360   Prolonged opening of mitochondrial permeability transition pore (mPTP) causes

361   mitochondria swelling, membrane potential dissipation and bioenergetic collapse, becoming a

362   determinant of cell death (Carraro et al., 2020). To test whether MTFP1 loss causes increased

363   susceptibility to mPTP opening, we assessed mitochondria swelling by exposing cardiac

364   mitochondria of pre-symptomatic WT and cMKO mice to a high concentration of Ca^{2+} and

365   kinetically measured the light scattering (Karch et al., 2013). Ca^{2+} overload induced an increased

366   mPTP dependent swelling of MTFP1-deficient cardiac mitochondria, which could be inhibited by

367   the mPTP inhibitor cyclosporin A (CsA), indicating that $Mtfp1$ deletion sensitizes cardiac

368   mitochondria to mPTP opening (Figure 4G-H). These findings were corroborated in $Mtfp1^{-/-}$ MEFs,

13

369 in which we observed increased mPTP sensitivity that could be suppressed by CsA treatment

370 (Figure S4A) or by knocking out Cyclophilin D (Cyp D, encoded by *Ppif*), the pharmacological

371 target of CsA in mitochondria (Figure 4I) (Halestrap and Davidson, 1990). Thus, these data clearly

372 indicate that loss of MTFP1 at the level of the IMM sensitizes mitochondria to mPTP opening.

373 To define the molecular mechanisms underlying the increased sensitivity PCD and mPTP opening

374 caused by MTFP1 ablation, we used WT and *Mtfp1*$^{-/-}$ MEFs. We began by confirming that like

375 *Mtfp1*$^{-/-}$ CMs, MEFs deleted of *Mtfp1* were more sensitive to PCD. As expected, *Mtfp1*$^{-/-}$ MEFs

376 showed increased sensitivity to multiple cell death stimuli, as evidenced by more rapid kinetics of

377 caspase 3/7 activation and cell death monitored by ML-assisted live-cell imaging of CellEvent (CE)

378 and Propodium Iodide (PI) uptake, respectively (Cretin et al., 2021). Treatment with cell death

379 triggers actinomycin D (ActD) and ABT-737 (Figure 4J-O), staurosporine (STS, figure S4B-D) or

380 DOXO (Figure 4P-R) all promoted a more rapid and robust cell death response in *Mtfp1*$^{-/-}$ MEFs

381 relative to WT MEFs, which could be blocked with the pan-caspase inhibitor Q-VD-OPh (qVD).

382 These effects were independent of cell proliferation or mitochondrial respiration, neither of which

383 were altered in *Mtfp1*$^{-/-}$ MEFs (Figure S4E, S2J-M). Taken together, our data clearly demonstrate a

384 protective role of MTFP1 in maintaining cell integrity and survival.

385

386 **Doxorubicin induced-cardiotoxicity accelerates the onset of cardiomyopathy in cMKO mice**

387 To test whether MTFP1 protected against PCD induction *in vivo,* we injected pre-symptomatic

388 (aged 8 weeks) cMKO and WT mice with DOXO and assessed cardiac function at 14 days post

389 treatment by echo (Figure S4F-J). Consistent with the data obtained *in vitro*, we observed that

390 DOXO accelerated the onset of cardiac dysfunction in cMKO mice by lowering LVEF (WT 60.85 ±

391 6.2% vs cMKO 47.02 ± 9.1%), PW thickness during systole (WT 1.082 ± 0.099 mm vs cMKO 0.887

392 ± 0.062 mm), while increasing systolic LV diameter (WT 2.393 ± 0.27 mm vs cMKO 3.009 ± 0.36

393 mm) and diastolic LV diameter (WT 3.505 ± 0.20 mm vs cMKO 3.918 ± 0.25 mm). These results

394 clearly indicate that cMKO mice are more susceptible to DOXO induced cardiotoxicity, accelerating

395 the onset of cardiomyopathy.

396

397 ***Inhibition of mPTP rescues cell death sensitivity of MTFP1 deficient cells***

14

398   It has been previously reported that DOXO mediates mPTP opening and cell death in lung cancer

399   cells (Lu et al., 2014) and cardiac myocytes, and that H_2O_2 activates necrosis through the induction

400   of mPTP opening (Vaseva et al., 2012). We observed that H_2O_2-induced cell death was

401   accelerated in $Mtfp1^{-/-}$ cells and was reduced, yet not totally abolished by caspase inhibition with

402   qVD, indicating that MTFP1 loss also renders cells more susceptible to caspase-independent cell

403   death (Figure 5A-C). Since MTFP1-deficient cardiac and MEF mitochondria were more susceptible

404   to mPTP opening (Figure 4G-I, S4A), we investigated whether prolonged mPTP opening

405   contributes to increased cell death sensitivity of MTFP1-deficient cells. To test the dependence of

406   PCD on Cyp D, we disrupted Cyp D in WT and $Mtfp1^{-/-}$ MEFs by introducing a truncating,

407   homozygous frame shift mutation (p.Val65*) by Crispr/Cas9 genome editing (Figure 5D) and

408   subjected cells to H_2O_2 (Figure 5E-G) or DOXO treatment (Figure 5H-J). By tracking the kinetics of

409   PI or CE uptake respectively, we observed that Cyp D ablation in $Mtfp1^{-/-}$ cells ($Mtfp1^{-/-}Ppif1^{-/-}$

410   MEFs) rescued the cell death sensitivity back to WT levels (Figure 5E-J). Consistent with a

411   cytoprotective effect of Cyp D ablation, we observed that the association of CsA to qVD treatment

412   had a synergic effect in suppressing cell death sensitivity of $Mtfp1^{-/-}$ MEFs to WT levels (Figure 5A-

413   C). Taken together, these results clearly indicate that loss of MTFP1 promotes mPTP opening via

414   Cyp D to lower the resistance to programmed cell death. To gain insights into the molecular

415   regulation of the mPTP by MTFP1 we sought to define the cardiac interactome of MTFP1. We

416   expressed FLAG-MTFP1 at the $Rosa26$ locus in C57Bl6/N mouse hearts via targeted transgenesis

417   (Figure S5A) and confirmed that the modest level of over-expression did negatively impact cardiac

418   function in vivo (Figure S5B-C). Next, we performed a co-immunoprecipitation study coupled to

419   mass spectrometry (MS) for the analysis of cardiac MTFP1 interactome. We identified 60

420   mitochondrial proteins besides the bait protein (MTFP1) that were exclusively present in FLAG-

421   MTFP1 eluates or significantly enriched greater than two-fold (Dataset EV3, Figure S5D). Among

422   these interactors we found factors involved in OXPHOS function (Figure S5E), notably proteins

423   required for the assembly and functions of Complex I (Ndufa10, NDUFA7, NDUFS6, NDUFB4,

424   NDUFS6, Mtnd5), Complex IV (CMC2, COX4I1, COX6B1, COX7A1, SCO2), and Complex V

425   (ATP5L, USMG5). In addition, we identified a number of proteins that have previously been

426   implicated in mPTP regulation including the ADP/ATP translocase SLC25A4 (Karch et al., 2019),

427   the inorganic phosphate carrier SLC25A3 (Kwong et al., 2014), and the heat shock protein TRAP1

15

428   (Kang et al., 2007) (Figure S5D-E). Altogether, our data have uncovered a functional and physical

429   link between MTFP1 and the mPTP complex in the inner mitochondrial membrane.

430

431   ***Discussion***

432

433   We initially chose to focus studies on Mitochondrial Fission Process 1 (MTFP1) because we

434   viewed this protein as a promising entry point to study the hitherto molecularly undefined process

435   of inner membrane division (Wai and Langer, 2016), based largely on previous studies that had

436   purported a pro-fission role upon over-expression and an anti-fission role upon depletion (Aung et

437   al., 2017a, 2017b; Duroux-Richard et al., 2016; Morita et al., 2017; Wang et al., 2017). While we

438   demonstrate MTFP1 to be a bona fide inner membrane protein in vivo (Figure S1B-C), confirming

439   previous in vitro studies (Tondera, 2005; Tondera et al., 2004), careful, unbiased mitochondrial

440   morphology analyses unequivocally excluded this protein as an essential fission factor (Figure 3G-

441   J) for the following reasons: 1) acute or chronic depletion of MTFP1 in vitro (Figure 3G-J) or

442   deletion in vivo (Figure 3C-D) had little impact on the elongation of the mitochondrial network and

443   2) MTFP1-deficient cells were not protected against mitochondrial fragmentation caused either by

444   accelerated fission or impaired fusion induced either by genetic or pharmacological triggers (Figure

445   3G-J). Consistent with these findings, we did not identify MTFP1 as a regulator of mitochondrial

446   morphology in a recent, comprehensive siRNA-based phenotypic imaging screens of all

447   mitochondrial genes performed in human fibroblasts (Cretin et al., 2021), which did identify

448   essential fission proteins like DRP1 and receptors (Fonseca et al., 2019; Losón et al., 2013;

449   Osellame et al., 2016), forcing us to reconsider the existing models of mitochondrial fission we (Ng

450   et al., 2021; Wai and Langer, 2016) and others had proposed (Giacomello et al., 2020). In

451   contrast, other studies have reported that chemical inhibitors of mTOR (Morita et al., 2017), PI3K

452   (Tondera et al., 2004), or miRNAs (Duroux-Richard et al., 2016; Wang et al., 2017) can deplete

453   MTFP1 protein levels and thus inhibit mitochondrial fragmentation, although the pleiotropic effects

454   of these molecules and the signaling cascades they regulate make it the interpretation of these

455   data very challenging. However, our in vitro studies confirmed that over-expression of MTFP1

456   does indeed promote mitochondrial fragmentation, which appears to be independent of stress-

457   induced OPA1 processing and alterations in the levels of the fission and fusion executors (Figure

16

458 S3B-C). In vivo, stable over-expression in cardiomyocytes does not appear to impact basal

459 cardiac function assessed by echocardiography (Figure S5C), although future studies will be

460 required to determine whether MTFP1 overexpression can impact cardiac physiology under stress

461 conditions.

462 If MTFP1 is dispensable for fission, what role, if any, does this metazoan-specific factor play in

463 mitochondria? Our in vivo studies revealed that cardiomyocyte-specific deletion of MTFP1 (cMKO)

464 drives the progressive development of dilated cardiomyopathy (DCM) beginning at 18 weeks of

465 age culminating in chronic heart failure and middle-aged death in both male and female mice.

466 Cardiac dysfunction was accompanied by a reduction in mitochondrial gene expression and

467 respiratory chain function, fibrotic remodeling (Figure 1P-R) and a general dysregulation of

468 metabolic genes (Figure 1Q), which are features that have been observed in other cardiomyocyte-

469 specific knockout mouse models of mitochondrial genes (Fernandez-Caggiano et al., 2020; Ghazal

470 et al., 2021; Hansson et al., 2004; Liao et al., 2015; Wai et al., 2015; Zhang et al., 2020b).

471 Similarly, accumulation of pathogenic mutations in mitochondrial DNA have recently been shown

472 to drive mitochondrial dysfunction and sterile inflammation in a number of different tissues

473 including the heart and genetic inhibition of the latter phenotype appears to resolve tissue

474 dysfunction, supporting a pathological role of cardiac inflammation triggered by mitochondrial

475 dysfunction(Lei et al., 2021). In cMKO mice, the aforementioned phenotypes were absent before

476 the onset of DCM, indicating that MTFP1 deletion in perinatal cardiomyocytes does not

477 compromise post-natal cardiac development nor function in mice. Thus, we hypothesize that the

478 metabolic and inflammatory remodeling that accompanies DCM manifests as downstream

479 response to cardiac dysfunction, which we are currently testing. Surprisingly, functional

480 characterization of field-stimulated primary adult cardiomyocytes from pre-symptomatic mice did

481 not reveal defects in contractile capacity, excitation contraction (EC) coupling, or sarcomere

482 integrity (Figure S1N-S), prompting us to search for other homeostatic dysfunctions of

483 cardiomyocytes that could account for the contractile defects of the beating heart caused by

484 MTFP1 deletion. Indeed, characterization of primary cardiomyocytes and cardiac mitochondria

485 from cMKO mice revealed an increased sensitivity to programmed cell death and increased

486 sensitivity to opening of the mitochondrial permeability transition pore (mPTP), respectively

487 (Baines et al., 2005; Carraro et al., 2020; Nakagawa et al., 2005). Accelerated opening of the

17

488 mPTP has been shown to control cardiomyocyte viability and cardiac function in genetic (Song et

489 al., 2015), infectious (Milduberger et al., 2021), and surgically-induced mouse models of

490 cardiomyopathy (Nakagawa et al., 2005). The identity of the mPTP has been hotly debated

491 (Carraro et al., 2020; Kwong and Molkentin, 2015; Morciano et al.) and a consensus has yet to be

492 achieved regarding its structure and molecular constitution, although compelling evidence from

493 knockout mice and in vitro reconstitution experiments have identified a number of mitochondrial

494 proteins associated with or integrated into the IMM subunits that are required for the efficient

495 opening of the mPTP including subunits of the ATP synthase, cyclophilin D (Cyp D, encoded by

496 the nuclear gene *Ppif*), and IMM carrier proteins of the SLC25 family (Baines et al., 2005; Basso et

497 al., 2008; Bernardi et al., 2015; Carraro et al., 2018, 2020; Karch et al., 2013, 2019; Kwong et al.,

498 2014; Nakagawa et al., 2005), several of which we identified by coimmunoprecipitation studies

499 performed on cardiac mitochondria to physically interact with FLAG-MTFP1, including SLC25A3

500 (Phosphate carrier), SLC25A4 (ANT1), TRAP1, ATP5L and USMG5 (Figure S5D-E).

501 Complexosome profiling of rat cardiac mitochondria revealed co-migration of MTFP1 with several

502 proteins we identified by coimmunoprecipitation (Heide et al., 2012), including SLC25A3,

503 SLC25A4, and Cyp D, implying that MTFP1 may act as a scaffold in the IMM to participate in the

504 maintenance, assembly or regulation of multi-protein complexes such as the mPTP complex. In

505 MTFP1-deficient cells, inhibiting mPTP opening by pharmacological inhibition with Cyclosporin A

506 (CsA) or genetic deletion of Cyp D rescues the sensitivity to mPTP opening and accelerated cell

507 death. Our discovery that the genetic deletion of *Mtfp1* sensitizes both post-mitotic cardiac cells

508 and mitotic epithelial cells to programmed cell death (PCD) without affecting cardiomyocyte

509 differentiation nor cell proliferation argues for a general role for MTFP1 in cell survival, which is

510 supported by studies in other cell lines (Duroux-Richard et al., 2016; Morita et al., 2017). Why

511 other groups have reported that MTFP1 depletion can protect gastric cancer and cardiomyocyte

512 cell lines from PCD induced by various cell death triggers including doxorubicin is unclear (Aung et

513 al., 2017a, 2017b; Wang et al., 2017). Although our in vivo data demonstrate that MTFP1 deletion

514 in cardiomyocytes accelerates, rather than retards, the cardiotoxic effects of doxorubicin (Figure

515 S4F-J), which is consistent with the PCD sensitivity we measured in MEFs and primary

516 cardiomyocytes, we cannot exclude that different cell lines and tissue may respond differently to

517 the loss of MTFP1.

18

518 Indeed, MTFP1 ablation significantly impacts mitochondrial respiration in cardiac cells but not in

519 highly glycolytic epithelial cells such as MEFs and human osteosarcoma cells (U2OS) (Figure S2J-

520 Q), in which the bioenergetic efficiency was unaffected.

521 Efficiently coupled oxidative phosphorylation requires proton gradient formed across the IMM by

522 the mitochondrial ETC, which is then harnessed by ATP synthase to generate ATP from ADP and

523 inorganic phosphate, imported into the matrix by the ADP/ATP translocase (ANT) and phosphate

524 carrier (SLC25A3), respectively. Mitochondrial uncoupling occurs when proton motive force is

525 dissipated by proton leak into the matrix and oxygen consumption is not coupled to ATP

526 generation. Maintenance of constant cellular ATP concentration is critical for cell survival and the

527 function, therefore, uncoupling of the ETC from ATP generation can have deleterious effects in

528 cardiac cells, whose constant energy supply is essential for the beating heart.

529 While the oxygen consumption rate (OCR) (Figure S2J-Q) and the maximal phosphorylating

530 respiration (Figure 2D, 2H, S2D, S2F), equivalent to state 3, were normal in cells and cardiac

531 mitochondria isolated from cMKO mice, MTFP1 loss significantly reduced the respiratory control

532 ratios (RCR) (Figure 2D, S2D) in cardiac mitochondria energized with complex I or complex II

533 substrates, suggesting a general mechanism of uncoupling of the respiration from the ATP

534 production as a result of increased proton leak trough the IMM.

535 Proton leak has marked influence on energy metabolism. Enhancement of this process in various

536 tissues can counteract the deleterious effects of nutrient overload via UCP1-dependent and

537 independent pathways (Roesler and Kazak, 2020) and thus may be beneficial in some settings. In

538 the heart, whose bioenergetic efficiency has evolved to maximize ATP output, excessive proton

539 leak has been shown to drive age-related cardiomyocyte and cardiac dysfunction in mice (Chiao et

540 al., 2020; Zhang et al., 2020a). Studies performed by the Rabinovitch lab clearly demonstrated that

541 ANT-dependent proton leak is increased in cardiomyocytes from old, but not young mice and can

542 be rejuvenated by blocking ANT and reducing sensitivity to mPTP opening.

543 In line with the notion that increased proton leak is maladaptive for the heart, our study shows for

544 the first time that MTFP1 loss in cardiomyocytes reduces the mitochondrial membrane potential as

545 a result of increased proton leak through the IMM (Figure 2D-E, S2D-G) preceding the onset of

546 cardiomyopathy. We provide direct evidence that ANT is the most likely site of proton leak in

547 cardiac mitochondria, as its inhibition with carboxyatractyloside (CATR) suppresses proton leak

548 and re-establishes normal membrane potential and respiratory control ratios in MTFP1-deficient

549 mitochondria (Figure 2H-J). While we have clear evidence of uncoupling via ANT on one hand

550 and increased sensitivity to mPTP opening and mitochondria swelling on the other, future studies

551 are still required to decipher whether these mechanisms are interdependent and whether they

552 must synergize to drive cardiac decline and heart failure. While a number of genetic mouse

553 models of cardiomyopathy targeting mitochondrial genes have been generated over the last 20

554 years, to the best of our knowledge cMKO mice represent the first in which bioenergetic efficiency

555 is compromised without affecting maximal respiratory capacity (state 3), thus providing a novel

556 model to study the relevance of cardiac mitochondrial uncoupling and its progressive impact on

557 cardiac homeostasis.

558 In summary our study reveals new and essential roles of MTFP1 in cardiac homeostasis that are

559 distinct from its previously reported impact on mitochondrial fission, the latter of which our data

560 conclusively show is unaffected in vitro and in vivo. Thus, our work now positions MTFP1 as a

561 critical regulator of mitochondrial coupling through ANT in cardiomyocytes and its loss leads to

562 membrane potential dissipation associated to mPTP opening, cell death and progressive DCM that

563 leads to heart failure and middle-aged death. These findings advance our understanding of the

564 mitochondrial defects that can trigger the development of dilated cardiomyopathy and heart failure.

565 We propose that MTFP1 to be a valuable tool for the molecular dissection of mitochondrial

566 uncoupling and mPTP function and thus a promising target to mitigate the pathological events of

567 cardiac and metabolic remodeling in heart disease.

568

569

570

571

572

573 **Figure Legends**

574 *Figure 1. **Mtfp1** deletion in cardiomyocytes causes dilated cardiomyopathy and middle-*

575 *aged death in mice*

576 **A)** AlphaFold prediction of MTFP1 as integral protein of the inner mitochondrial membrane (IMM)

577 associated with mitochondrial fission. DRP1 binds to its receptors MFF or MiD49/51 to initiate

578 mitochondrial constriction. IMM fission occurs coincidently with mtDNA replication mediated by

579 TFAM and POLG2. S-OPA1 accumulation generated by OMA1 accelerates fission.

580 **B)** Generation of a cardiomyocyte-specific *Mtfp1* KO (cMKO) mouse model.

581 **C)** *Mtfp1* mRNA expression measured by bulk RNAseq (arbitrary units; AU) in heart tissue of WT

582 (n=5) and cMKO (n=5) mice at 8 weeks (Dataset EV2). Data represent mean ± SD; 2-tailed

583 unpaired Student's t-test, ****p<0.0001.

584 **D)** Densitometric quantification of immunoblot analysis of cardiac lysates from WT (n=5) and

585 cMKO (n=5) mice at 8 weeks using the indicated antibodies. Data represent mean ± SD; Unpaired

586 t-test, **p<0.01.

587 **E)** MTFP1 protein expression in cardiac tissue of WT (n=4) and cMKO (n=4) at 18 weeks

588 measured by label free quantification (LFQ) mass spectrometry (MS) (Dataset EV1). Data

589 represent mean ± SD; 2-tailed unpaired Student's t-test, ***p<0.001.

590 **F)** Kaplan-Meier survival curve of WT (n=9) and cMKO (n=15) male mice. Median lifespan of

591 cMKO mice is 26.4 weeks. Log-rank (Mantel-Cox) test, ****p < 0.0001.

592 **G-L)** Longitudinal echocardiography of WT and cMKO mice from 10 to 34 weeks of age.

593 **G)** Representative M-Mode echocardiographic images of left ventricles from WT (left) and cMKO

594 (right) of male mice at 34 weeks.

595 **H)** Quantification of left ventricular ejection fraction (% LVEF) of WT and cMKO mice at indicated

596 ages. Data represent mean ± SD; 2way Anova - Sidak's multiple comparison test: 10 week WT

597 (n=13) vs cMKO (n=18); 14 week WT (n=4) vs cMKO (n=6); 18 week WT (n=10) vs cMKO (n=13)

598 ***p<0.001; 22 week WT (n=4) vs cMKO (n=6) **p<0.01; 30 week WT (n=3) vs cMKO (n=7)

599 **p<0.01; 34 week WT (n=4) vs cMKO (n=10)****p<0.0001.

600 **I)** Quantification of systolic interventricular septum thickness (IVSs, mm) of WT and cMKO mice at

601 indicated ages. Data represent mean ± SD; 2way Anova - Sidak's multiple comparison test, 18

602 weeks ***p<0.001; 22 weeks *p<0.05; 34 weeks ***p<0.001.

21

J) Quantification of left ventricle posterior wall thickness at systole (LVPWs, mm) of WT and cMKO mice at indicated ages. Data represent mean ± SD; 2way Anova - Sidak's multiple comparison test, 18 weeks **p<0.01; 22 weeks *p<0.05; 30 weeks ***p<0.001, 34 weeks ****p<0.0001.

K) Quantification of left ventricle end diastolic diameter (LVDD, mm) of WT and cMKO mice at indicated ages. Data represent mean ± SD; 2way Anova - Sidak's multiple comparison test, 34 week ****p<0.0001.

L) Quantification of left ventricle end systolic diameter (LVSD, mm) of WT and cMKO mice at indicated ages. Data represent mean ± SD; 2way Anova - Sidak's multiple comparison test, 30 weeks *p<0.05; 34 weeks ***p<0.001.

M) Representative histological images of cardiac short axis view of WT (n=4) and cMKO (n=4) at 34 weeks. H&E (left), Massons's Trichrome (middle) and Picrosirius red (right) staining show cardiac remodeling and collagen deposition within the myocardium of cMKO mice. Scale bar 500 μM.

N) Circulating levels of cardiac troponin-I (cTNI) measured in serum of WT and cMKO mice at 18 [WT (n=6) vs cMKO (n=6)] and 34 weeks [WT (n=11) vs cMKO (n=20)]. Data represent mean ± SD; 2-tailed unpaired Student's t-test at 18 weeks and 34 weeks (w); ***p<0.001.

O) Myosin light chain 1 (MLC-1) levels measured in serum of WT and cMKO mice at 18 [WT (n=5) vs cMKO (n=6)] and 34 weeks (w) [WT (n=11) vs cMKO (n=17)]. Data represent mean ± SD; 2-tailed unpaired Student's t-test at 18w and 34w; **p<0.01 and ***p<0.001.

P) Volcano plots generated from the RNAseq analysis (Dataset EV2) of the differentially expressed genes in cardiac tissue of WT and cMKO mice at 8 (left) and 18 weeks (right).

Q) Number of genes up-regulated and down-regulated in cMKO mice at 8 (blue) and 18 (pink) weeks (w) within the gene ontology (GO) term: metabolic process (left), mitochondrial genes (MitoCarta, middle) and inflammation (right) obtained from RNAseq analysis (Dataset EV2).

R) mRNA expression measured by bulk RNAseq (arbitrary units; AU) of the indicated profibrotic genes in heart tissue of WT (n=6) and cMKO (n=6) mice at 18 weeks. Data represent mean ± SD; 2-tailed unpaired Student's t-test.

Figure 2. *Mtfp1 is required for bioenergetic efficiency in cardiac mitochondria*

A) Substrates from fatty acid oxidation (mustard) and glycolysis (purple, blue) are metabolized in the TCA cycle which delivers fuels the electron transport chain (ETC) complexes located in the inner mitochondrial membrane by providing NADH and FADH to complexes I (purple) and II (blue), respectively. Complexes I, III and IV extrude protons from matrix into the intermembranous space creating an electrochemical gradient driving the phosphorylation of ADP at the ATP synthase (complex V). The electron flow is limited by the availability of oxygen, a terminal acceptor of the energy depleted electron at the complex IV (cytochrome oxidase). Uncoupling proteins such as ANT promote a proton leak, playing an important role in regulation of membrane potential and oxidative phosphorylation efficiency. Specific inhibitors of complex I (rotenone), complex V (oligomycin), and ANT (carboxyatractyloside, CATR).

B) Oxygen consumption rates (JO_2) measured by high-resolution respirometry of cardiac mitochondria from WT (n=5) and cMKO (n=5) male mice at 18 weeks. Complex I driven respiration (left) was measured in presence of pyruvate, malate, glutamate (PGM) and ADP followed by the addition of rotenone and succinate to assess complex II driven respiration (middle) and antimycin A, carbonyl cyanide m-chlorophenyl hydrazine (CCCP), and N,N,N′,N′-Tetramethyl-p-phenylenediamine (TMPD) and ascorbate to measure complex IV driven respiration (right). Data represent mean ± SD; unpaired Student's t-test, $*p<0.05$.

C) Oxygen consumption rates (JO_2) measured by high-resolution respirometry of cardiac mitochondria from WT (n=5) and cMKO (n=5) male mice at 34 weeks (w). Complex I driven respiration (left) was measured in presence of pyruvate, malate, glutamate (PGM) and ADP followed by the addition of rotenone and succinate to assess complex II driven respiration (middle) and antimycin A, carbonyl cyanide m-chlorophenyl hydrazine (CCCP), and N,N,N′,N′-Tetramethyl-p-phenylenediamine (TMPD) and ascorbate to measure complex IV driven respiration (right). Data represent mean ± SD; unpaired Student's t-test, $*p<0.05$.

D) Oxygen consumption rates (JO_2) measured by high-resolution respirometry of cardiac mitochondria isolated from WT (n=11) and cMKO (n=11) mice between 8-10 weeks (left). Respiration was measured in presence of pyruvate, malate, and glutamate (PGM) (state 2) followed by the addition of ADP (state 3) and Oligomycin (Omy- state 4). Data represent mean ± SD. Multiple t-test, state 2 $***p<0.001$, state 4 $*p<0.05$. Respiratory control ratios (RCR) of state

23

662   3:2 (middle: JO_2 ADP/PGM) and respiratory control ratios (RCR) of state 3:4 (right: JO_2 ADP/Omy).

663   Data represent mean ± SD; 2-tailed unpaired Student's t-test, ***p<0.001.

664   **E)** Mitochondrial membrane potential ($\Delta\Psi$) measured by quenching of Rhodamine 123 (RH123)

665   fluorescence in cardiac mitochondria isolated from WT (n=11) and cMKO (n=11) mice between 8-

666   10 weeks. $\Delta\Psi$ was measured in presence of pyruvate, malate, and glutamate (PGM) (state 2)

667   followed by the addition of ADP (state 3) and Oligomycin (state 4). Data represent mean ± SD;

668   Multiple t-test, ****p<0.0001.

669   **F)** Representative BN-PAGE immunoblot analysis of cardiac OXPHOS complexes isolated from

670   WT and cMKO mice at 8-10 weeks using the indicated antibodies.

671   **G)** Equal amounts of protein extracted from WT (n=5) and cMKO (n=5) hearts between 8-10

672   weeks were separated by SDS–PAGE and immunoblotted with the indicated antibodies and

673   quantified by densitometry using VINCULIN as a loading control. Data represent mean ± SD.

674   **H)** Oxygen consumption rates measured by high-resolution respirometry (left; JO_2) and

675   mitochondrial membrane potential (right; $\Delta\Psi$) measured by quenching of Rhodamine 123 (RH123)

676   fluorescence in cardiac mitochondria of WT (n=4) and cMKO (n=4) mice between 8-10 week of

677   age. JO_2 and $\Delta\Psi$ were measured in presence of pyruvate, malate, and glutamate (state 2) followed

678   by the addition of ADP (state 3) and carboxyatractyloside (CATR) (state 4). Data represent mean

679   ± SD; Multiple t-test, ***p<0.001.

680   **I)** Oxygen consumption rates measured by high-resolution respirometry (left; JO_2) and

681   mitochondrial membrane potential (right; $\Delta\Psi$) measured by quenching of Rhodamine 123 (RH123)

682   fluorescence in cardiac mitochondria of WT and cMKO mice between 8-10 week of age.

683   Respiration was measured in presence of pyruvate, malate, and glutamate (PGM) (state 2)

684   followed by the addition of ADP (state 3), Oligomycin (state 4) and carboxyatractyloside (state 4-

685   CATR) [WT (n=3) cMKO (n=3)]. Data represent mean ± SD. Multiple t-test, state 2 ***p<0.001,

686   state 4 *p<0.05.

687   **J)** Respiratory control ratio (RCR) of state 3:4 (ADP/CATR) between WT (n=4) and cMKO (n=4)

688   calculated from H). Data represent mean ± SD.

689   **K)** Mitochondrial membrane potential ($\Delta\Psi$) measured by quenching of Rhodamine 123 (RH123)

690   fluorescence in cardiac mitochondria of WT and cMKO mice between 8-10 week of age. $\Delta\Psi$ was

691   measured in presence of pyruvate, malate, and glutamate (state 2) followed by the addition of ADP

24

692 (state 3), oligomycin (state 4) and GTP (state 4 - GTP) [WT (n=3), cMKO (n=3)]. Data represent

693 mean ± SD; Multiple t-test, *p<0.05, ***p<0.001, ****p<0.0001.

694

695 ***Figure 3. MTFP1 is dispensable for mitochondrial fission.***

696 **A)** Representative confocal images of primary adult cardiomyocytes isolated from WT and cMKO

697 mice at 8 weeks. Mitochondria were stained with MitoTracker Deep Red (MTDR) and

698 tetramethylrhodamine, ethyl ester (TMRE), nuclei were stained with NucBlue (NB). Scale bar=50

699 μm.

700 **B)** Violin plot of mitochondrial content (MTDR Intensity/Area) of WT (n=6085) and cMKO CMs

701 (n=3647) measured in A).

702 **C)** Representative transmission electron micrographs of cardiac posterior walls of WT (top, n=3)

703 and cMKO (bottom, n=3) mice at 8-10 weeks. Scale bar: 500 nm.

704 **D)** Violin plot of mitochondrial surface area (μm^2) within cardiac posterior wall measured in C (WT

705 mitochondria n=659; cMKO mitochondria n=966). Dotted line represents quartiles and dashed line

706 represents median; **p<0.01 Mann-Whitney test.

707 **E)** Mitochondrial DNA (mtDNA) content in WT (n=5) and cMKO (n=5) heart tissue quantified by

708 amplification of the mitochondrial *Mttl1* gene relative to nuclear gene *b-Actin*. Data represent mean

709 ± SD.

710 **F)** Immunoblot of mitochondrial fission and fusion proteins. Equal amounts of protein from cardiac

711 WT and cMKO (8-10 week) extracts were separated by SDS–PAGE and immunoblotted with the

712 indicated antibodies (horizontal line denotes different membranes). VINCULIN or ACTIN are used

713 as loading controls.

714 **G)** Representative confocal images of WT and *Mtfp1$^{-/-}$* MEFs treated with the fission inducing

715 drugs: oligomycin (Omy), Rotenone, H_2O_2 and carbonyl cyanide m-chlorophenyl hydrazine

716 (CCCP). Mitochondria were stained with MitoTracker Deep Red (MTDR, green) and nuclei with

717 NucBlue (NB, blue). Scale bar=100 μm.

718 **H)** Quantification of mitochondrial morphology in G) by supervised ML using WT cells with normal

719 (UT), fragmented (CCCP-treated) or hypertubular (cycloheximide-treated) mitochondria as ground

720 truths. Data are means ± SEM of 4 independent replicates. 2way-ANOVA, Dunnet's multiple

721 comparison test: % fragmentation ****p<0.0001 treatment vs WT UT or *Mtfp1$^{-/-}$* UT.

25

I) Representative confocal images of WT and *Mtfp1*$^{-/-}$ MEFs treated with indicated siRNAs (20 nM) for 72 h. Mitochondria were stained with MitoTracker Deep Red (MTDR, green) and nuclei with NucBlue (NB, blue). Scale bar=100 μm.

J) Quantification of mitochondrial morphology in I) by supervised machine learning (ML) using WT cells with normal (non-targeting NT siRNA), fragmented (*Opa1* siRNA) or hypertubular (*Dnm1l* siRNA) mitochondria as ground truths. Data are means ± SEM of 4-8 technical replicates. 2way-ANOVA, Dunnet's multiple comparison test: % hypertubular * $p<0.05$; *** $p<0.001$ versus WT NT siRNA; % fragmented **** $p<0.0001$ versus *Mtfp1*$^{-/-}$ NT siRNA.

Figure 4. MTFP1 protects against mitochondrial PTP opening and cell death

 A) Representative confocal images of adult cardiomyocytes (CMs) isolated from WT and cMKO at 8 weeks stained with tetramethylrhodamine, ethyl ester (TMRE) treated with or without cyanide m-chlorophenyl hydrazine treatment (CCCP) for 15 minutes. Rod-shaped CMs: live cells, round-shaped CMs: dead cells. Scale bar: 500 μm.

B) Quantification of number of live cells (% survival) in A) by supervised machine learning. Data are means ± SD of n=3 independent experiments. Unpaired Student's t-test; * $p<0.05$.

C) Representative confocal images of adult cardiomyocytes (CMs) isolated from WT and cMKO at 8 weeks stained with tetramethylrhodamine, ethyl ester (TMRE) and subjected to H_2O_2 treatment for 1 hour. Rod-shaped CMs: live cells, round-shaped CMs: dead cells. Scale bar: 500 μm.

D) Quantification of number of live cells (% survival) over time measured in C) by supervised machine learning. Data are means ± SD of 2-3 culture replicates and representative of n=3 experiments. 2wayANOVA, Tukey's multiple comparison test, *** $p<0.001$, **** $p<0.0001$ vs WT H_2O_2.

E) Representative confocal images of adult cardiomyocytes (CMs) isolated from WT and cMKO at 8 weeks stained with tetramethylrhodamine, ethyl ester (TMRE) and subjected to Doxorubicin (DOXO). Scale bar: 500 μm.

F) Quantification of number of live cells (% survival) in E) by supervised machine learning. Data are means ± SD of 2-3 culture replicates and representative of n=3 experiments. 2wayANOVA, Tukey's multiple comparison test, * $p<0.05$, ** $p<0.01$, *** $p<0.001$, **** $p<0.0001$ vs WT DOXO. Scale bar: 1 mm.

26

G) Mitochondrial permeability transition pore (mPTP) opening. Swelling assay performed on cardiac mitochondria extracted from hearts of WT (n=3) and cMKO (n=3) mice at 8-10 weeks. Light scattering (absorbance 540 nm, % relative to T_0] was measured every 20 s before and after addition of a single pulse of $CaCl_2$ (arrowhead). Cyclosporin A (CsA) was added prior $CaCl_2$ pulse to inhibit mPTP-induced mitochondrial swelling. Data are means ± SD.

H) one-way ANOVA of maximal absorbance$_{540\ nm}$ (% relative to T_0) change in G) *p<0.05, ****p<0.0001.

I) Mitochondrial permeability transition pore (mPTP) opening. Swelling assay performed on mitochondria purified from WT and *Mtfp1$^{-/-}$, Ppif$^{-/-}$* and *Mtfp1$^{-/-}$Ppif$^{-/-}$* MEFs. Mitochondrial absorbance changes (absorbance 540 nm, % relative to T_0) are measured every 20 s prior and after addition of a single pulse of $CaCl_2$ (arrowhead). Cyclosporin A (CsA) was added prior Ca^{2+} to inhibit mPTP-dependent swelling. Data are means ± SD.

J) Representative confocal images of WT and *Mtfp1$^{-/-}$* MEFs subjected to actinomycin D (ActD) *plus* ABT-737 treatment in the presence or absence of the pan-caspase inhibitor q-VD-OPh hydrate (qVD). Cell death was monitored by using nuclear Propidium Iodide uptake (PI, orange) and imaging cells every hour (h) for 20h. Scale bar = 100 µm.

K) Kinetics of PI uptake was determined by counting the number of PI$^+$ positive cells (orange) over total number cells nuclear stained with NucBlue (NB, blue) and expressed as % PI$^+$/NucBlue. Data are means ± SD of n=4 independent experiments.

L) one-way ANOVA of K) at 18h, ****p<0.0001.

M) Representative confocal images of WT and *Mtfp1$^{-/-}$* MEFs subjected to actinomycin D (ActD) plus ABT-737 treatment in the presence or absence of the pan-caspase inhibitor q-VD-OPh hydrate (qVD). Live induction of the caspase 3/7 activation was monitored by using the CellEvent (CE, green) reagent and imaging cells every hour (h) for 20h. Scale bar = 100 µm.

N) Kinetics of caspase 3/7 activation was determined by counting the number of CE$^+$ positive cells (green) over total number cells nuclear stained with NucBlue (NB, blue) and expressed as % CE$^+$/NucBlue. Data are means ± SD of n=4 independent experiments.

O) one-way ANOVA of N) at 12h, ****p<0.0001.

P) Representative confocal images of WT and *Mtfp1$^{-/-}$* MEFs subjected to doxorubicin treatment in the presence or absence of the pan-caspase inhibitor q-VD-OPh hydrate (qVD). Live induction of

27

782   the caspase 3/7 activation was monitored by using the CellEvent (CE, green) reagent and imaging

783   cells every hour (h) for 18h. Scale bar = 100 μm.

784   **Q)** Kinetics of caspase 3/7 activation was determined by counting the number of CE$^+$ positive cells

785   (green) over total number cells nuclear stained with NucBlue (NB, blue) and expressed as %

786   CE$^+$/NucBlue. Data are means ± SD and representative of at least n=3 independent experiments.

787   **R)** one-way ANOVA of Q) at 12h, p<0.0001.

788

789   **Figure 5. *mPTP accounts for cell death sensitivity in MTFP1 deficient cells***

790   **A)** Representative confocal images of WT and *Mtfp1$^{-/-}$* MEFs subjected to H$_2$O$_2$ treatment. The

791   pan-caspase and cyclophilin D inhibitors, q-VD-OPh hydrate (qVD) and cyclosporin A (CsA)

792   respectively, were used to block both caspase and mPTP dependent cell death. Cell death was

793   monitored by Propidium Iodide uptake (PI, orange) and imaging cells every hour (h) for 18h. Scale

794   bar = 100 μm.

795   **B)** Kinetics of PI uptake was determined by counting the number of PI$^+$ positive cells (orange) over

796   total number cells nuclear stained with NucBlue (NB, blue) and expressed as % PI$^+$/NucBlue. Data

797   are means ± SD of n=6 independent experiments.

798   **C)** one-way ANOVA of B) at 18h, *p<0.05

799   **D)** Validation of Cyclophilin D (CYP D) deletion by Crispr/Cas9 genome editing in WT and *Mtfp1$^{-/-}$*

800   MEFs. Equal amounts of protein extracted from WT, *Mtfp1$^{-/-}$*, *Ppif$^{-/-}$*, *Mtfp1$^{-/-}$ Ppif$^{-/-}$* MEFs were

801   separated by SDS–PAGE and immunoblotted with the indicated antibodies. SDHA was used as

802   mitochondrial marker and loading control.

803   **E)** Representative confocal images of WT, *Mtfp1$^{-/-}$*, *Ppif$^{-/-}$*, *Mtfp1$^{-/-}$ Ppif$^{-/-}$* MEFs subjected to H$_2$O$_2$

804   treatment. Cell death was monitored by Propidium Iodide uptake (PI, orange) and imaging cells

805   every hour (h) for 18h. Scale bar = 100 μm.

806   **F)** Kinetics of PI uptake was determined by counting the number of PI$^+$ positive cells (orange) over

807   total number cells nuclear stained with NucBlue (NB, blue) and expressed as % PI$^+$/NucBlue. Data

808   are means ± SD of n=3 independent experiments.

809   **G)** one-way ANOVA of F) at 18h; **p<0.01, ****p<0.0001.

810   **H)** Representative confocal images of WT, *Mtfp1$^{-/-}$*, *Ppif$^{-/-}$*, *Mtfp1$^{-/-}$ Ppif$^{-/-}$* MEFs subjected to

811   doxorubicin (DOXO) treatment. Live induction of the caspase 3/7 activation was monitored by

28

812   using the CellEvent (CE, green). CellEvent positive cells (CE$^+$, green) over total number over cells

813   NucBlue labeled (blue) were imaged every hour (h) for 18h. Scale bar = 100 μm.

814   **I)** Kinetics of caspase 3/7 activation was determined by counting the number of CE$^+$ positive cells

815   (green) over total number cells nuclear stained with NucBlue (NB, blue) and expressed as %

816   CE$^+$/NucBlue. Data are means ± SD and representative of n=3 independent experiments.

817   **J)** one-way ANOVA of I) at 16h, ****$p<0.0001$.

818

819   **Figure 6. Model for the regulation of mitochondrial and cardiac function by MTFP1**

820   *Mtfp1* deletion in cardiomyocytes occurs at birth (cMKO) and sensitizes cardiac myocytes to

821   mitochondrial permeability transition pore (mPTP) opening, cell death and increases mitochondria

822   uncoupling of the inner membrane. At the adult age of 8-10 weeks heart of cMKO mice have

823   normal structure and function but undergoes to the development of a progressive dilated

824   cardiomyopathy (DCM) at 18 weeks which progresses to severe heart failure and middle-aged

825   death by 34 weeks. At onset of DCM, cMKO mice exhibit increased cardiac cell death, reduced

826   mitochondrial respiration, and induction of a sterile inflammatory response.

827

828

829   *Figure S1*. ***Mtfp1* deletion in cardiomyocytes causes dilated cardiomyopathy and middle-**

830   **aged death in mice**

831   **A)** Genotype tissue expression plot **(**GTEx) of MTFP1 in human tissues.

832   **B)** Alkaline carbonate extraction assay demonstrating solubility of MTFP1 similar to other multi-

833   pass integral membrane proteins. Immunoblot analysis of soluble (S) and insoluble (pellet, P)

834   fractions of wild type (WT) cardiac mitochondria extracted with Na_2CO_3 at the indicated pH. SDHA,

835   SDHB and MT-CO2, ANT1, NDUFA9 were used as markers for soluble and integral membrane

836   proteins, respectively.

837   **C)** Determination of sub-mitochondrial localization of MTFP1 in cardiac mitochondria by protease K

838   protection assay. TOMM40 and MFN2, were used as OMM markers, CYT C as an IMS marker,

839   and ANT1, ATP5B and SDHA as IMM markers.

840   **D)** Targeting strategy for conditional inactivation of mouse *Mtfp1*. To allow deletion of *Mtfp1* exons

841   2 and 3 were flanked in both cases by LoxP sites (blue arrowheads). Flox denotes NeoR cassette

29

842   containing LoxP targeted locus. LoxP denotes NeoR cassette-deleted targeted locus. Δ denotes

843   deletion induced by Cre-recombinase. FRT sites (green) initially flank NeoR cassette (yellow).

844   **E)** Kaplan-Meier survival curve of WT (n=11) and cMKO (n=14) female mice. Median lifespan of

845   cMKO mice is 37.5 weeks. Log-rank (Mantel-Cox) test, ***p<0.001.

846   **F)** M-Mode echocardiography images of WT (top) and cMKO (bottom) female mice at 34 weeks.

847   **G)** Quantification of left ventricular ejection fraction (% LVEF) of WT (n=7) and cMKO (n=6) female

848   mice at 34 weeks. Data represent mean ± SD. 2-tailed unpaired Student's t-test, ****p<0.0001.

849   **H)** Quantification of systolic interventricular septum thickness (IVSs, mm) of WT (n=7) and cMKO

850   (n=6) female mice at 34 weeks. Data represent mean ± SD. 2-tailed unpaired Student's t-test,

851   *p<0.05.

852   **I)** Quantification of systolic left ventricular posterior wall thickness (LVPWs, mm) of WT (n=7) and

853   cMKO (n=6) female mice at 34 weeks. Data represent mean ± SD. 2-tailed unpaired Student's t-

854   test, ***p<0.001.

855   **J)** Quantification of left ventricle end systolic diameter (LVSD, mm) of WT (n=7) and cMKO (n=6)

856   female mice at 34 weeks. Data represent mean ± SD. 2-tailed unpaired Student's t-test,

857   ***p<0.001.

858   **K)** Quantification of left ventricle end diastolic diameter (LVDD, mm) of WT (n=7) and cMKO (n=6)

859   female mice at 34 weeks. Data represent mean ± SD. 2-tailed unpaired Student's t-test,

860   ***p<0.001.

861   **L)** Quantification of pulmonary edema. Wet Lung/Body Weight (BW) of WT (n=8) and cMKO (n= 8)

862   at 34 weeks. Data represent mean ± SD; 2-tailed unpaired Student's t-test, *p<0.05.

863   **M)** Representative images (left) of WT (top) and cMKO (bottom) hearts isolated from female mice

864   at 34 weeks; (right) quantification of ratio of heart mass to tibia length (mg/mm). Data represent

865   mean ± SD, 2-tailed unpaired Student's t-test, ***p<0.001.

866   **N-S)** Isolated primary adult cardiomyocytes from WT (n=51) and cMKO (n=52) mice at 8 weeks

867   were i) field-stimulated at 0.5 Hz, ii) exposed to the β-adrenergic agonist isoproterenol and iii)

868   stimulated at frequency of 5 Hz, iv) and then stepped back to 0.5 Hz washing out (wo)

869   isoproterenol. **N)** Diastolic and systolic sarcomere length (μm) of WT and cMKO; **O)** fractional

870   sarcomere shortening; **P)** Time to 50% or 90% decay of sarcomere shortening in WT or cMKO

871   myocytes, ***p<0.001.

Q-S) Isolated primary adult cardiomyocytes from WT (n=29) and cMKO (n=52) mice at 8 weeks were i) field-stimulated at 0.5 Hz, ii) exposed to the β-adrenergic agonist isoproterenol and iii) stimulated at frequency of 5 Hz, iv) and then stepped back to 0.5 Hz washing out (wo) isoproterenol. Intracellular Ca^{2+} concentrations ($[Ca^{2+}]_c$) were assessed by loading cells with Indo-1 AM and recording calcium transients at 405 nm/485 nm. **Q)** $[Ca^{2+}]_c$ at diastole or systole; **R)** amplitude of $[Ca^{2+}]_c$ transients; **S)** Time to 50% or 90% decay (RT) of $[Ca^{2+}]_c$ in WT and cMKO myocytes, **p<0.01, ****p<0.0001.

Figure S2. Mtfp1 is required for bioenergetic efficiency in cardiac mitochondria

A) Equal amounts of protein extracted from WT (n=4) and cMKO (n=6) hearts at 18 weeks were separated by SDS–PAGE and immunoblotted with the indicated antibodies.

B) Volcano plot of the Label Free Quantification of the cardiac proteome in WT and cMKO mice (18 weeks) listed in Dataset EV1.

C) Ratio of NAD(P)H/FAD of the redox states of NAD(P)H/NAD(P)$^+$ and FADH$_2$/FAD assessed in field-stimulated WT (n=51) and cMKO (n=51) cardiomyocytes isolated from 8-10 weeks old mice (n=3).

D) Oxygen consumption rates (left; JO$_2$) measured by high-resolution respirometry of cardiac mitochondria isolated from WT (n=5) and cMKO (n=5) mice between 8-10 weeks. Respiration was measured in presence of succinate and rotenone (state 2) followed by the addition of ADP (state 3) and Oligomycin (Omy- state 4). Data represent mean ± SD. Multiple t-test, state 2 ***p<0.001, state 4 *p<0.05. Respiratory control ratios (RCR) of state 3:2 (middle; ADP/Succinate (SUCC)) and state 3:4 (right; ADP/Omy) under complex-II driven respiration. Data represent mean ± SD; multiple t-test, *p<0.05.

E) Mitochondrial membrane potential (ΔΨ) measured by quenching of Rhodamine 123 (RH123) fluorescence in cardiac mitochondria from WT (n=8) and cMKO (n=8) mice between 8-10 weeks. ΔΨ was measured in presence of rotenone and succinate (state 2) followed by the addition of ADP (state 3) and Oligomycin (state 4). Data represent mean ± SD; Multiple t-test, *p<0.05, ***p<0.001.

F) Oxygen consumption rates (JO$_2$) measured by high-resolution respirometry of cardiac mitochondria isolated from WT (n=6) and cMKO (n=6) mice between 8-10 weeks. Respiration was

31

measured in presence of malate (state 2) followed by the addition of ADP (state 3) and palmitoyl-carnitine (PC). Data represent mean ± SD.

G) Mitochondrial membrane potential ($\Delta\Psi$) measured by quenching of Rhodamine 123 (RH123) fluorescence in cardiac mitochondria isolated from WT (n=6) and cMKO (n=6) mice between 8-10 weeks. $\Delta\Psi$ sustained by fatty acid oxidation was measured in presence of malate (state 2) followed by the addition of ADP (state 3) and palmitoyl-carnitine (PC). Data represent mean ± SD; Multiple t-test, ***p<0.001.

H) PCR genotyping of *Mtfp1* alleles in mice. Deletion of exons 2 and 3 was obtained by crossing *Mtfp1*[LoxP/LoxP] mice with *CMV-Cre* recombinase mice to generate heterozygous knockout *Mtfp1*^{+/-} offspring. Agarose gel of PCR amplicons of genomic DNA. The wild type (387 bp) and the deleted (737 bp) alleles are shown for *Mtfp1*^{+/+} and *Mtfp1*^{-/-} cells.

I) Equal amounts of protein extracted from WT and *MTFP1*[Crispr] U2OS cells separated by SDS–PAGE and immunoblotted with antibodies against MTFP1 and normalized against Stain Free as a loading control.

J-M) Mitochondrial respiration measured in adherent wild type (WT) and *Mtfp1*^{-/-} immortalized mouse embryonic fibroblasts (MEFs) cells using the Seahorse Flux Analyzer. **J)** Oxygen consumption rate (OCR) normalized to protein concentration under **K)** Basal **L)** Maximal (FCCP) and **M)** non-phosphorylating (state 4) respiration (Oligomycin treated - Omy). Data are means ± SD of n=4 independent experiments measured on different days. Each point represents the mean of 7-12 technical OCR measurements replicates of each independent experiment.

N-Q) Mitochondrial respiration measured in adherent wild type (WT) and *MTFP1*[Crispr] human U2OS osteosarcoma cells using the Seahorse Flux Analyzer. **N)** Oxygen consumption rate (OCR) normalized to protein concentration under **O)** Basal **P)** Maximal (FCCP) and **Q)** non-phosphorylating (state 4) respiration (Oligomycin treated - Omy). Data are means ± SD of 7-12 technical replicates.

R) Inhibition of proton leak by MTFP1. Proposed model of the regulation of ANT-dependent proton leak by MTFP1 (red). Proton gradient generated by the electron transport chain (ETC) is harnessed by ATP synthase in WT cells to generate ATP from ADP and Pi. Upon Mtfp1 ablation (*Mtfp1*^{-/-}), ANT-mediated proton leak increases thus compromising bioenergetic efficiency.

32

931 *Figure S3. MTFP1 is dispensable for mitochondrial fission.*

932 **A)** Immunoblot of mitochondrial fission and fusion proteins in WT and *Mtfp1$^{-/-}$* MEFs. Equal

933 amounts of protein extracted from WT and *Mtfp1$^{-/-}$* MEFs were separated by SDS–PAGE and

934 immunoblotted with the indicated antibodies (horizontal line denotes different

935 membranes). VINCULIN was used as loading control.

936 **B)** Representative confocal images of fragmented mitochondria morphology in MEFs stably

937 expressing FLAG-MTFP1 (mitoYFP, green). EV (empty vector, top), FLAG-MTFP1 (bottom).

938 Scale bar=100 μm.

939 **C)** Representative immunoblot of mitochondrial fission (red) and fusion (green) proteins in WT and

940 FLAG-MTFP1 stably overexpressing MEFs. Equal amounts of protein were separated by SDS–

941 PAGE and immunoblotted with the indicated antibodies (horizontal line denotes different

942 membranes).

943

944 *Figure S4. MTFP1 protects against mitochondrial PTP opening and cell death*

945 **A)** Mitochondrial permeability transition pore (mPTP) opening. Swelling assay performed on

946 mitochondria purified from WT and *Mtfp1$^{-/-}$* MEFs. Mitochondrial absorbance changes (absorbance

947 540 nm, % relative to T_0) are measured every 20 s prior and after addition of a single pulse of

948 CaCl$_2$ (arrowhead). Cyclosporin A (CsA) was added prior Ca^{2+} to inhibit mPTP-dependent swelling.

949 Data are means ± SD.

950 **B)** Representative confocal images of WT and *Mtfp1$^{-/-}$* MEFs subjected to staurosporine (STS)

951 treatment in the presence or absence of the pan-caspase inhibitor q-VD-OPh hydrate (qVD). Cell

952 death was monitored by measuring Propidium Iodide uptake (PI) and imaging cells every hour (h)

953 for 18 h. Scale bar = 100 μm.

954 **C)** Kinetics of PI uptake was determined by counting the number of PI$^+$ positive cells (orange) over

955 total number cells nuclear stained with NucBlue (NB, blue) and expressed as % PI$^+$/NucBlue. Data

956 are means ± SD of n=4 independent experiments.

957 **D)** one-way ANOVA of C) at 12h, ****$p<0.0001$.

958 **E)** Cell proliferation curves of WT and *Mtfp1$^{-/-}$* MEFs in glucose (4.5 g/L) containing medium.

959 Number of cells was determined by counting the number of NucBlue (NB) labeled nuclei every 24

960 h.

33

F) Representative M-Mode echocardiographic images of left ventricles of WT (left) and cMKO (right) mice treated with doxorubicin (Doxo, cumulative 20 mg/kg) at 10 weeks.

G) Quantification of left ventricular ejection fraction (% LVEF) of WT (n=5) and cMKO (n=5) after 2 weeks of Doxo administration. Data represent mean ± SD. 2-tailed unpaired Student's t-test, *p<0.05.

H) Quantification of systolic left ventricular diameter (LVSD, mm) of WT (n=5) and cMKO (n=5) mice after Doxo treatment. Data represent mean ± SD. 2-tailed unpaired Student's t test, *p<0.05.

I) Quantification of diastolic left ventricular diameter (LVDD, mm) of WT (n=5) and cMKO (n=5) mice after Doxo treatment. Data represent mean ± SD. 2-tailed unpaired Student's t test, *p<0.05.

J) Quantification of systolic left ventricular posterior wall thickness (LVPWs, mm) of WT (n=5) and cMKO (n=5) mice after Doxo treatment. Data represent mean ± SD. 2-tailed unpaired Student's t test, *p<0.05.

Figure S5. Generation of FLAG-MTFP1 mouse model to define the cardiac interactome

A) For inducible overexpression of mCherry-P2A-Flag-Mtp18, two mouse models were generated from one construct. The first (upper pane) allowing inducible expression from the CAG-promoter, the second (lower panel) from the mouse Rosa26 promoter. To do so, the construct in the upper panel is generated and recombined into the mouse Rosa26 locus. The genuine Rosa26 promoter is further upstream, and its transcript is spliced into the splice acceptor of exon 2 ("s.acc.", purple). In the native state, transcription is aborted at the insulator site (H19, black), and instead started at the CAG promoter (pCAG, yellow arrow). The loxP-flanked (lox, blue arrow heads) neo–STOP cassette for conditional activation has a stop site that is a large region of SV40 intron plus late polyA (neo, green arrow; STOP, blue box). The cDNA is inserted downstream of the neo/stop cassette. Both, Rosa26-driven and CAG-driven expression, is polyadenylated at a bovine growth hormone polyA site (bGH pA, small black box). For exchange of the promoters, the CAG-cassette is flanked by FRT-sites. This cassette will be excised by Flp-mediated deletion in vivo, leaving mCherry-P2A-Flag-Mtp18 expression under control of the Rosa26 promoter. Upon Cre mediated deletion, the mCherry-P2A-Flag-Mtp18 cDNA is expressed from the CAG promoter (upper panel) or the intrinsic Rosa26 promoter (lower panel).

B) Representative immunoblot of the expression of Flag-MTFP1 compared to endogenous MTFP1 levels in KI mice.

C) Quantification of left ventricular ejection fraction (% LVEF) of WT (n=4) and KI (n=3) mice at 20 weeks. Data represent mean ± SD.

D) Volcano plot of the FLAG-MTFP1 interactome analyzed by mass spectrometry. Mitochondrial proteins exclusively present in FLAG-MTFP1 eluates or significantly enriched greater than two-fold, listed in Dataset EV3.

E) Functional classification of 60 mitochondrial proteins identified in Co-IP eluates in C) (Dataset EV3).

1003 **Material and Methods**

1004 **Animals**

1005 Animals were handled according to the European legislation for animal welfare (Directive

1006 2010/63/EU). All animal protocols were reviewed and approved by the local and national

1007 authorities. Mice were housed within a specific pathogen free facility and maintained under

1008 standard housing conditions of a 14-10h light-dark cycle, 50-70% humidity, 19-21°C with free

1009 access to food and water in cages enriched with bedding material and gnawing sticks. *Mtfp1*

1010 conditional mice (*Mtfp1*$^{LoxP/LoxP}$) were generated by PolyGene AG (Switzerland) on a C57Bl6/N

1011 background. Cardiomyocyte specific *Mtfp1* KO mice (cMKO; *Myh6-Cre*$^{tg/+}$*Mtfp1*$^{LoxP/LoxP}$) were

1012 generated by crossing *Mtfp1* conditional mice (*Mtfp1*$^{LoxP/LoxP}$) with transgenic (Tg) mice expressing

1013 the Cre recombinase under the control of the cardiac alpha myosin heavy chain 6 promoter (*Myh6-*

1014 *Cre*)(Agah et al., 1997). Littermates that were homozygous for the conditional allele and negative

1015 for *Myh6-Cre* were used as controls (WT; *Myh6-Cre*$^{+/+}$*Mtfp1*$^{LoxP/LoxP}$). Heterozygous whole-body

1016 *Mtfp1* KO mice (*Mtfp1*$^{+/-}$) were generated by crossing *Mtfp1* conditional mice (*Mtfp1*$^{LoxP/LoxP}$) with

1017 transgenic (Tg) mice expressing the Cre recombinase under the control of the CMV promoter

1018 (*CMV-Cre*)(Schwenk et al., 1995) and backcrossing to C57Bl6/N wild type (WT) mice.

1019 Cardiomyocyte specific FLAG-MTFP1 Knock-In (KI) mice (*Myh6-Cre*$^{tg/+}$*Mtfp1*$^{+/+}$, *CAG*$^{tg+/}$) were

1020 generated by crossing an inducible mouse model for mCherry-P2A-FLAG-MTFP1 generated by

1021 PolyGene AG (Switzerland) on a C57Bl6/N background expression under the CAG promoter with

1022 mice expressing the Cre recombinase under the control of the cardiac alpha-(α) myosin heavy

1023 chain 6 promoter (*Myh6-Cre*).

1024

1025 **Cell Lines**

1026 WT (*Mtfp1*$^{+/+}$) and knockout (KO) *Mtfp1*$^{-/-}$ embryos were isolated at E13.5 following F1

1027 heterozygous intercrosses of *Mtfp1*$^{+/-}$ whole-body KO mice. Immortalization of WT (*Mtfp1*$^{+/+}$) and

1028 *Mtfp1*$^{-/-}$ primary mouse embryonic fibroblasts (MEFs) was performed as previously

1029 described(Cretin et al., 2021, 2021) using a plasmid encoding SV40 large T antigen. MEFs cells

1030 were maintained in Dulbecco's modified Eagle's medium (DMEM + GlutaMAX, 4.5 g/L D-Glucose,

1031 pyruvate) supplemented with 5% FBS and 1% penicillin/streptomycin (P/S, 50 μg/ml) in a 5% CO_2

1032 atmosphere at 37°C.

36

1033 Genetic disruption of *Ppif* in WT and *Mtfp1⁻ᐟ⁻* MEFs was performed via CRISPR-Cas9 gene editing

1034 targeting Exon 1 of *Ppif* (sgRNA: forward: aaacCCGGGAACCCGCTCGTGTAC and reverse:

1035 CACCGTACACGAGCGGGTTCCCGG. sgDNA oligonucleotides were annealed and cloned into

1036 pSpCas9(BB)-2A-GFP PX458 to generate pTW363 (pSpCas9(BB)-2A-GFP PPIFsgDNA).   WT

1037 (*Mtfp1⁺ᐟ⁺*) and *Mtfp1⁻ᐟ⁻* immortalized MEFs were transfected with 2.5 µg of plasmid pTW363 using

1038 Lipofectamine 2000 (Life Technologies). After 48h incubation, cells were individually isolated in 96

1039 well plates by FACS. Clones were then expanded and validated by Sanger sequencing and

1040 western blotting. Both single Ppif KO MEFs (*Ppif⁻ᐟ⁻*) and double KO *Mtfp1⁻ᐟ⁻Ppif⁻ᐟ⁻* cells carry the

1041 same homozygous c.126delG insertion that is predicted to yield a truncated polypeptide product at

1042 amino acid position 65 (1-64 protein) p.Val65*. Immunoblot analysis was used to confirm the

1043 absence of PPIF protein.

1044 MEFs expressing mitochondrially targeted YFP (mitoYFP) were generated from

1045 Gt(ROSA26)Sor^mitoYFP/+ embryos on a C57Bl6/N genetic background at E13.5 and immortalized

1046 using a plasmid encoding SV40 large T antigen as previously described(Cretin et al., 2021). MEFs

1047 stably expressing FLAG-MTFP1 were generated by lentiviral transduction with pTW142 (pLVX-

1048 EF1α-MTFP1) containing a puromycin resistant marker. The empty vector (EV) pLVX-EF1α

1049 (pTW122) was used to generate control cells.

1050 Human U2OS osteosarcoma cells were depleted for MTFP1 by CRISPR-Cas9 gene editing. The

1051 single-guide RNAs (sgRNAs) were designed using the CRISPR-Cas9 design tool (benchling.com)

1052 to target Exon 1 of *MTFP1.* sgDNA oligonucleotides (forward: 5'-

1053 caccgGCGCAGAGCGCGATCTCTAC -3' and reverse: 5'-aaacGTAGAGATCGCGCTCTGCGCc-

1054 3') were annealed and cloned into the BbsI digested pSpCas9(BB)-2A-GFP vector (SpCas9(BB)-

1055 2A-GFP (PX458) which was a gift from Feng Zhang (Addgene plasmid # 48138). U2OS cells were

1056 transfected in 6-well dishes with 2ug of pSpCas9(BB)-2A-GFP plasmid containing the respective

1057 sgRNA using Lipofectamine 2000 (Life Technologies, 11668027). After 24h incubation, GFP

1058 positive cells were individually isolated by fluorescence-activated cell sorting. Clones were

1059 expanded and were validated by western blotting and DNA sequencing.

1060

1061 **SDS-PAGE immunoblot analysis**

37

1062   Immunoblot analysis was used to assess steady-state protein levels in cardiac tissue and cell

1063   lysates. For tissue lysates, mice were sacrificed by cervical dislocation, the chests were opened,

1064   and the hearts were excised, weighed, flash frozen in liquid nitrogen, and stored at -80°C until use.

1065   The LV tissue or MEFs cellular pellet was homogenized in cold RIPA buffer [1 mg/ 20 µL, 1%

1066   Triton X-100, 1% sodium deoxycholate, 0.1% SDS, 150 mM NaCl, 50 mM Tris·HCl (pH 7.8), 1 mM

1067   EDTA, and 1 mM EGTA] in presence of protease and phosphatase inhibitors and kept on ice for

1068   30 minutes. The homogenate was then centrifuged for 15 min at 16,000g, 4°C. The protein

1069   concentration was determined by Bradford assay (Bio-Rad) using a BSA standard curve. The

1070   protein absorbance was measured at 595 nm by using a microplate reader Infinite M2000 (Tecan).

1071   Equal amounts of protein were reconstituted in 4x Laemmli Sample Buffer [355 mM, 2-

1072   mercaptoethanol, 62.5 mM Tris-HCl pH 6.8, 10% (v/v) glycerol, 1%(w/v) SDS, 0.005% (v/v)

1073   Bromophenol Blue] and heated at 95°C for 5 min. Samples (10 µg) were resolved on 4-20%

1074   polyacrylamide gels (Mini Protean TGX Stain-Free gels, BioRad) and transferred to nitrocellulose

1075   membrane with Trans-Blot® Turbo™ Transfer system (Bio-Rad). Equal protein amount across

1076   membrane lanes were checked by Ponceau S staining or Stain-free detection. Membranes were

1077   blocked for at least 1h with 5% (w/v) semi-skimmed dry milk dissolved in Tris-buffered saline

1078   Tween 0.1% (TBST), incubated overnight at 4°C with primary antibodies dissolved 1:1,000 in 2%

1079   (w/v) Bovine Serum Albumin (BSA), 0.1% TBST. The next day membranes were incubated in

1080   secondary antibodies conjugated to horseradish peroxidase (HRP) at room temperature for 2h

1081   (diluted 1:10,000 in BSA 2% TBST 0.1%). Finally, membranes were incubated in Clarity™ Western

1082   ECL Substrate (Bio-Rad) for 2 min and luminescence was detected using the ChemiDoc® Gel

1083   Imaging System. Densitometric analysis of the immunoblots was performed using Image Lab

1084   Software (Bio-Rad).

1085

1086   **Mitochondrial isolation**

1087   Isolated cardiac mitochondria were freshly isolated as previously described (Mourier et al., 2014)

1088   with some modifications. Briefly, the heart was washed in ice-cold PBS solution. Ventricles were

1089   separated from atria and non-myocardial tissue, cut in small pieces, and then transferred to an ice-

1090   cold 2-ml homogenizer (Teflon pestle) and manually homogenized in IB buffer (sucrose 275 mM,

1091   Tris 20 mM, EGTA-KOH 1 mM, pH 7.2) containing Trypsin-EDTA (0.05%). Trypsin activity was

1092   then inhibited by adding to the homogenate bovine serum albumin (BSA) fatty acid free (0.25

1093   mg/mL) and protease inhibitor cocktail (PIC, Roche).

1094   Mitochondria isolation from MEFs was performed starting from 10 x 150 mm dishes at 100%

1095   confluence. Cells were collected into 10 mL of IB Buffer containing BSA fatty acid free (0.25

1096   mg/mL) and PIC and homogenized with 30 stokes of the plunger at 1500 rpm on ice.

1097   Cardiac and/or cellular homogenates were then centrifuged at low speed (1000 g, 10 min, 4 °C) to

1098   discard nuclei and debris, and further centrifuged (3200 g, 15 min, 4°C) to obtain the crude

1099   mitochondrial pellet and the cytosolic fraction. The crude mitochondrial pellet was finally

1100   resuspended in IB buffer containing BSA and PIC and protein concentration was determined by

1101   using the Bradford assay.

1102

1103   **Protease Protection Assay**

1104   Crude mitochondria isolated from WT mouse hearts was subjected to protease protection assay as

1105   previously described (Anand et al., 2014). 50 µg of crude mitochondria were resuspended into the

1106   following buffers without protease inhibitors: 1) Mitochondrial isolation IB buffer 2) Mitochondrial

1107   isolation buffer with Proteinase K (100 µg/mL) 3) Swelling buffer (EDTA 1 mM, HEPES 40 mM) 4)

1108   Swelling buffer + Proteinase K (100 µg/mL) 5) Swelling buffer + Proteinase K (100 µg/ml) + Triton

1109   X-100 0.5% and incubated at 37°C for 30 minutes at 750 rpm. Mitochondrial proteins were then

1110   precipitated in trichloric acid buffer (14% TCA , 40 mM HEPES, 0.02% Triton X-100) for 3 hours at

1111   -20°C and centrifugated for 20 min. Pellets were washed twice with ice-cold acetone and air-dried

1112   prior to re-suspension in 1x Laemilli sample buffer (Bio-Rad) for SDS-PAGE and immunoblot

1113   analysis.

1114

1115   **Alkaline Carbonate Extraction**

1116   Alkaline carbonate extraction of membrane proteins was performed as previously described

1117   (Anand et al., 2014). Crude mitochondria isolated from WT mouse hearts were resuspended and

1118   incubated for 30 min on ice with 0.1 M Na_2CO_3 at the following pH: 12.5, 11.5, 10.5, or 9.5. The

1119   suspensions were ultra-centrifuged at 4°C for 30 min at 90,000 g in Beckman polycarbonate tubes

1120   in a TLA 110 rotor. Supernatants and pellets were then incubated in trichloric acid buffer (14%

1121   TCA, 40 mM HEPES, 0.02% Triton X-100) for 15 min on ice, followed by centrifugation for 20 min

1122   at 28,000 g at 4°C. The samples were washed 3x with 100% acetone, subsequently dried for 30

1123   min at RT. The dried pellet was then resuspended with 1x Laemilli sample buffer (Bio-Rad) for

1124   SDS-PAGE and western blot analysis.

1125

1126   siRNA transfection

1127   Silencing of the indicated genes was performed using forward transfection: 20 nM of the indicated

1128   SmartPool siRNAs listed in Dataset EV4 were mixed with Lipofectamine RNAiMax (Invitrogen),

1129   added on top of cells seeded in 6-well dishes (300,000 cells/well) and incubated at 37°C in a CO_2

1130   incubator. For live imaging experiments, cells were seeded in 96 well plates (Cell Carrier Ultra,

1131   Perkin Elmer) 48h after transfection to perform live imaging after 72h post-transfection.

1132

1133   Cardiac RNA sequencing and RT-qPCR

1134   WT and cMKO mice aged 8 and 18 weeks were sacrificed by cervical dislocation and hearts were

1135   quickly excised and rinsed with cold sterile PBS. Left ventricle posterior walls were collected and

1136   snap frozen in liquid nitrogen and stored at -80°C until use. Total RNA was extracted by using

1137   TRIzol (Invitrogen, NY, USA) according to standard procedures. The Trizol/chloroform mixture was

1138   centrifuged at 12000g for 15 min at 4°C, the supernatant corresponding to the aqueous phase was

1139   transferred to a new tube, mixed with ethanol 70%, and then applied to an RNA mini-column

1140   extraction kit (NucleoSpin RNA kit, MACHEREY-NAGEL) according to the manufacturer's

1141   recommendations. After DNA digestion, total RNA was eluted with RNase-free water and stored in

1142   liquid nitrogen. RNA was quantified by using the Bioanalyzer 2100 (Agilent) and only RNA samples

1143   (≥ 50 ng/µL) with an RNA integrity value (RIN) ≥ 6.8, $OD^{260/280}$ ≥ 2, $OD^{260/230}$ ≥ 2 were considered

1144   for the transcriptome profiling. For RNA sequencing, libraries were built using a TruSeq Stranded

1145   mRNA library Preparation Kit (Illumina, USA) following the manufacturer's protocol. Two runs of

1146   RNA sequencing were performed for each library on an Illumina NextSeq 500 platform using

1147   single-end 75bp. The RNA-seq analysis was performed with Sequana 0.8.5(Cokelaer et al., 2017)

1148   using an RNA-seq pipeline 0.9.13 (https://github.com/sequana/sequana_rnaseq) built on top of

1149   Snakemake 5.8.1(Köster and Rahmann, 2012). Reads were trimmed from adapters using

1150   Cutadapt 2.10(Martin, 2011) then mapped to the mouse reference genome GRCm38 using STAR

1151   2.7.3a(Dobin et al., 2013). FeatureCounts 2.0.0 was used to produce the count matrix, assigning

1152 reads to features using annotation from Ensembl GRCm38_92 with strand-specificity

1153 information(Liao et al., 2014). Quality control statistics were summarized using MultiQC 1.8(Ewels

1154 et al., 2016). Statistical analysis on the count matrix was performed to identify differentially

1155 expressed genes (DEGs), comparing WT and cMKO. Clustering of transcriptomic profiles were

1156 assessed using a Principal Component Analysis (PCA). Differential expression testing was

1157 conducted using DESeq2 library 1.24.0 scripts based on SARTools 1.7.0(Varet et al., 2016)

1158 indicating the significance (Benjamini-Hochberg adjusted p-values, false discovery rate FDR <

1159 0.05) and the effect size (fold-change) for each comparison.

1160 For RT-qPCR, 1 µg of total RNA was converted into cDNA using the iScript Reverse Transcription

1161 Supermix (Bio-Rad). RT-qPCR was performed using the CFX384 Touch Real-Time PCR Detection

1162 System (Bio-Rad) and SYBR® Green Master Mix (Bio-Rad) using the primers listed in Dataset

1163 EV1. Gapdh was amplified as internal standard. Data were analyzed according to the 2−ΔΔCT

1164 method(Livak and Schmittgen, 2001).

1165

1166 **Proteomics**

1167 Heart extract proteins were extracted and denatured in RIPA buffer. Samples were sonicated using

1168 a Vibracell 75186 and a miniprobe 2 mm (Amp 80% // Pulse 10 off 0.8, 3 cycles) and further

1169 centrifuged. Protein assay was performed on supernatant (Pierce 660 nm, according to

1170 manufacturer instructions) and 100 µg of each extract was delipidated and cleaned using a

1171 Chloroform / Methanol / Water precipitation method. Briefly, 4 volume of ice-cold methanol were

1172 added to the sample and vortex, 2 volume of ice-cold chloroform were added and vortex and 3

1173 volume of ice-cold water was added and vortex. Samples were centrifuged 5 min at 5000 g. The

1174 upper layer was removed and proteins at the interface were kept. Tubes were filled with ice-cold

1175 methanol and centrifuged at max speed for 5 min. Resulting protein pellet was air-dried and then

1176 dissolved in 130 µl of 100mM NaOH before adding 170 µl of Tris 50 mM pH 8.0, tris (2-

1177 carboxyethyl)phosphine (TCEP) 5 mM and chloroacetamide (CAA) 20 mM. The mixture was

1178 heated 5 min at 95 °C and then cooled on ice. Endoprotease LysC (1µg) was use for a 8h

1179 digestion step at (37° C) followed with a trypsin digestion (1 µg) at 37°C for 4 h. Digestion was

1180 stopped adding 0.1% final of trifluoroacetic acid (TFA). Resulting peptides were desalted using a

1181 C18 stage tips strategy (Elution at 80% Acetonitrile (ACN) on Empore C18 discs stacked in a P200

41

1182 tips) and 30 µg of peptides were further fractionated in 4 fractions using

1183 poly(styrenedivinylbenzene) reverse phase sulfonate (SDB-RPS) stage-tips method as previously

1184 described(Kulak et al., 2014; Rappsilber et al., 2007). Four serial elutions were applied as

1185 following: elution 1 (80 mM Ammonium formate (AmF), 20% (v/v) ACN, 0.5% (v/v) formic acid

1186 (FA)), elution 2 (110 mM AmF, 35% (v/v) ACN, 0.5% (v/v) FA), elution 3 (150 mM AmmF, 50%

1187 (v/v) ACN, 0.5% (v/v) FA) and elution 4 (80% (v/v) ACN, 5 % (v/v) ammonium hydroxide). All

1188 fractions were dried and resuspended in 0.1% FA before injection.

1189 NanoLC-MS/MS

1190 LC-MS/MS analysis of digested peptides was performed on an Orbitrap Q Exactive Plus mass

1191 spectrometer (Thermo Fisher Scientific, Bremen) coupled to an EASY-nLC 1200 (Thermo Fisher

1192 Scientific). A home-made column was used for peptide separation (C_{18} 50 cm capillary column

1193 picotip silica emitter tip (75 µm diameter filled with 1.9 µm Reprosil-Pur Basic C_{18}-HD resin, (Dr.

1194 Maisch GmbH, Ammerbuch-Entringen, Germany)). It was equilibrated and peptide were loaded in

1195 solvent A (0.1 % FA) at 900 bars. Peptides were separated at 250 nl.min^{-1}. Peptides were eluted

1196 using a gradient of solvent B (ACN, 0.1 % FA) from 3% to 7% in 8 min, 7% to 23% in 95 min, 23%

1197 to 45% in 45 min (total length of the chromatographic run was 170 min including high ACN level

1198 step and column regeneration). Mass spectra were acquired in data-dependent acquisition mode

1199 with the XCalibur 2.2 software (Thermo Fisher Scientific, Bremen) with automatic switching

1200 between MS and MS/MS scans using a top 12 method. MS spectra were acquired at a resolution

1201 of 35000 (at m/z 400) with a target value of 3×10^6 ions. The scan range was limited from 300 to

1202 1700 m/z. Peptide fragmentation was performed using higher-energy collision dissociation (HCD)

1203 with the energy set at 27 NCE. Intensity threshold for ions selection was set at 1×10^6 ions with

1204 charge exclusion of z = 1 and z > 7. The MS/MS spectra were acquired at a resolution of 17500 (at

1205 m/z 400). Isolation window was set at 1.6 Th. Dynamic exclusion was employed within 45 s.

1206 Data Processing

1207 Data were searched using MaxQuant (version 1.5.3.8) using the Andromeda search

1208 engine(Tyanova et al., 2016) against a reference proteome of Mus musculus (53449 entries,

1209 downloaded from Uniprot the 24th of July 2018). The following search parameters were applied:

1210 carbamidomethylation of cysteines was set as a fixed modification, oxidation of methionine and

1211 protein N-terminal acetylation were set as variable modifications. The mass tolerances in MS and

42

1212 MS/MS were set to 5 ppm and 20 ppm respectively. Maximum peptide charge was set to 7 and 5

1213 amino acids were required as minimum peptide length. A false discovery rate of 1% was set up for

1214 both protein and peptide levels. All 4 fractions per sample were gathered and the iBAQ intensity

1215 was used to estimate the protein abundance within a sample(Schwanhäusser et al., 2011). The

1216 match between runs features was allowed for biological replicate only.

1217 For this large-scale proteome analysis part, the mass spectrometry data have been deposited at

1218 the ProteomeXchange Consortium (http://www.proteomexchange.org) via the PRIDE partner

1219 repository(Perez-Riverol et al., 2019; Vizcaíno et al., 2014) with the dataset identifier PXD028516

1220

1221 **mtDNA content quantification**

1222 Genomic DNA was extracted using the NucleoSpin Tissue (MACHEREY-NAGEL) and quantified

1223 with NanoQuant Plate™ (Infinite M200, TECAN). RT-qPCR was performed using the Real-Time

1224 PCR Detection System (Applied Biosystems StepOnePlus), 20 ng of total DNA and the SYBR®

1225 Green Master Mix (Bio-Rad). b-*Actin* was amplified as an internal, nuclear gene standard as

1226 previously described(Cretin et al., 2021). PCR primer sequences are listed in Dataset EV4. Data

1227 were analyzed according to the $2^{-\Delta\Delta CT}$ method(Livak and Schmittgen, 2001).

1228

1229 **Mitochondrial imaging and quantification in MEFs**

1230 MEFs cells were seeded on 96-well or 384-well CellCarrier Ultra imaging plates (Perkin Elmer) 24h

1231 before imaging. Nuclei were stained with NucBlue™ Live ReadyProbes™ Reagent (ThermoFisher

1232 Scientific) at 1 drop per 10 mL of media. Fluorescent labeling of mitochondria was achieved using

1233 MitoTracker DeepRed (MTDR) at 100 nM for 30 min at 37°C, 5% CO_2. Cells were then washed

1234 with regular medium and images were acquired using the Operetta CLS or Opera Phenix High-

1235 Content Analysis systems (Perkin Elmer), with 20x Water/1.0 NA, 40x Air/0.6 NA, 40x Water/1.1

1236 NA or 63x Water/1.15 NA. MTDR (615-645 nm) and NucBlue (355-385 nm) were excited the

1237 appropriate LEDs (Operetta CLS) or lasers (Opera Phenix). Automatic single-cell classification of

1238 non-training samples (i.e. unknowns) was carried out by the supervised machine-learning (ML)

1239 module using Harmony Analysis Software (PerkinElmer) as previously described(Cretin et al.,

1240 2021).

1241

Analysis of oxygen consumption

Oxygen consumption of intact cells or crude mitochondria was measured with the XFe96 Analyzer (Seahorse Biosciences) and High Resolution Respirometry (O2k-Fluorespirometer, Oroboros, AT), respectively. For Seahorse experiments, cells (experimentally optimized density of 20,000 cells/well for MEFs and U2OS cells) were seeded onto 96-well XFe96 cell culture plates. On the following day, cells were washed and incubated with Seahorse XF Base Medium completed with 1 mM Pyruvate, 2 mM Glutamine and 10 mM Glucose. Cells were washed with the Seahorse XF Base Medium and incubated for 45 min in a 37°C non-CO_2 incubator before starting the assay. Following basal respiration, cells were treated sequentially with: oligomycin 1 µM, CCCP 2 µM and antimycin A plus rotenone (1 µM each) (Sigma). Measurements were taken over 2-min intervals, proceeded by a 1-min mixing and a 30s incubation. Three measurements were taken for the resting OCR, three for the non-phosphorylating OCR, three for the maximal OCR and three for the extramitochondrial OCR. After measurement, the XFe96 plate was washed with Phosphate-Buffered Saline (PBS) and protein was extracted with RIPA for 10 min at RT. Protein quantity in each well was then quantified by Bicinchoninic acid assay (BCA) by measuring absorbance at 562 nm and used to normalize OCR measurements as previously described(Cretin et al., 2021).

For O2k respirometry, isolated cardiac mitochondria were freshly isolated from adult WT and cMKO mice (8, 18 or 34 weeks) as described above. Simultaneous measurement of mitochondrial respiration and membrane potential ($\Delta\psi$) was assessed by O2K-Fluorometry using a O2K-Fluorescence LED2-Module operated through the amperometric channel of the O2K. Briefly, 25 or 50 µg of cardiac mitochondria were resuspended in Mir05 buffer [$MgCl_2$-$6H_2O$ 3 mM, Lactobionic Acid 60 mM, Taurine 20 mM, KH_2PO_4 10 mM, Hepes-KOH 20 mM, Sucrose 110 mM, EGTA-KOH 0.5 mM, BSA (1g/L)] in presence of Rhodamine 123 (RH-123) (0.66 µM). Maximal mitochondrial respiration capacity (OXPHOS) was determined under consecutive administrations of PGM [pyruvate 10 mM, glutamate 5 mM, malate 5 mM, state 2] or malate (2 mM) and palmitoyl-carnitine (10 µM) in presence of ADP (1 mM, state 3) to assess complex I-driven respiration; rotenone (0.5 µM) and succinate (10 mM, state 2) for the measurement of complex II-driven respiration; antimycin A (2.5 µM), ascorbate (2 mM), N,N,N',N'-tetramethyl-p-phenylenediamine (TMPD, 0.5 mM) and carbonyl cyanide m-chlorophenyl hydrazone (CCCP, 2 µM) for the determination of the complex IV-driven respiration. The addition of oligomycin (Omy, 25 nM) or carboxyatractyloside

44

1272 (CATR, 1 µM) was used to determine the non-phosphorylating respiration (state 4). Cytochrome *c*

1273 (2 µM) – mediated O_2 flux was used to evaluate the integrity of the OMM following the

1274 mitochondria isolation. Respiratory control ratios (RCR) of state 3: state 4 were used to evaluate

1275 the integrity of the IMM. RH-123 fluorescence quenching (Δ fluorescence) in energized

1276 mitochondria was used as a direct measurement of $\Delta\psi$.

1277

1278 **Echocardiography**

1279 Transthoracic echocardiographic acquisitions were performed by using a Vevo 3100 Imaging

1280 System coupled to a 25-55 MHz linear-frequency transducer (MX550D, FUJIFILM VisualSonics).

1281 Randomized WT and cMKO mice [10 to 34 weeks of age (male), 34 weeks (female) were

1282 anesthetized and maintained with 2% isofluorane in oxygen, placed in a supine position on a 37°C

1283 warmed pad. Limb electrodes and a rectal probe were used to monitor define (ECG) and body

1284 temperature. Before echocardiography and the addition of the pre-warmed ultrasound gel, thorax

1285 fur was removed using hair-removal cream. To assess the overall left ventricle (LV) size and LV

1286 function, B- and M-Mode images were acquired in parasternal long axis view (PLAX) between 400-

1287 500 bpm. The systolic and diastolic LV dimensions [interventricular septum thickness (IVS; mm),

1288 LV diameter (LVD; mm), LV posterior wall thickness (LVPW; mm)] and cardiac output [ejection

1289 fraction (% EF)] were determined by acquiring and analyzing at least 3 independent cardiac cycles

1290 within at least 3 M-Mode images.

1291

1292 **Doxorubicin Treatment**

1293 WT and cMKO mice aged 8 weeks received a cumulative dose of 20 mg/kg of doxorubicin (Doxo,

1294 2 intra-peritoneal injections of 10 mg/kg/saline, given at 3-day intervals; control mice received

1295 saline injections). Transthoracic echocardiography was performed at day 14 post treatment. Body

1296 weight was recorded every 3 days and a loss higher than 20% was considered as endpoint of the

1297 study.

1298

1299 **Determination of serum levels of cardiac troponin I and cardiac MLC1**

1300 A mouse ELISA kit was used to compare serum levels of cardiac troponin I (cTnI, Life Diagnostics)

1301 and cardiac myosin light chain 1 (MLC1, Life Diagnostic) in WT and cMKO male mice aged 18 and

45

1302   34 weeks. Blood was collected via submandibular vein puncture from non-anesthetized mice, left

1303   for 30 min at RT and then centrifuged at 5,000 g at 4°C for 10 min then snap-frozen into liquid

1304   nitrogen. Serum was stored at -80°C until next use. The assays to determine cTnI and MLC1

1305   levels were performed following the exact manufacturer's instructions.

1306

1307   **Histology**

1308   WT and cMKO mice aged 34 weeks were sacrificed by cervical dislocation and the hearts excised

1309   post-mortem. The whole hearts were then fixed with Formol 4 % (VWR chemicals) overnight and

1310   then fully dehydrated by a series of ethanol gradients. Tissues were then paraffin-embedded and

1311   sectioned in a short view at a thickness of 4 µm on a microtome. The sections were de-paraffinized

1312   in xylene and rehydrated followed by hematoxylin and eosin (H&E), Masson's trichrome or

1313   Picrosirius Red staining according to the standard protocols.

1314

1315   **Transmission Electron Microscopy**

1316   Transmission electron microscopy was performed on cardiac tissue from WT and cMKO mice

1317   aged 8-10 weeks. Small pieces (1x1x1 mm) from the left ventricle posterior wall were fixed in a

1318   37°C prewarmed mix of PHEM 1x buffer (60 mM PIPES, 25 mM HEPES, 10 mM EGTA, 2 mM

1319 $MgCl_2$; pH 7.3), 2.5% glutaraldehyde and 2% PFA for 30 min, followed by an overnight fixation at

1320   4°C. Specimens were then rinsed 3 times with PHEM 2X buffer. Samples were incubated with 1 %

1321   osmium tetroxide (Merck) and 1.5 % ferrocyanide (Sigma Aldrich) in 0.1M PHEM. After

1322   dehydration by a graded series of ethanol, samples were gradually infiltrated at RT with epoxy

1323   resin and after heat polymerization, sections with a thickness of 70 nm were cut with a Leica UCT

1324   microtome and collected on carbon, formvar coated copper grids. Sections were contrasted with

1325   4% aqueous uranylacetate and Reynold's lead citrate. Generation of ultra-large electron

1326   microscopy montages at a magnification of 14500x (pixel size = 6.194 nm, bin 1, US4000

1327   Ultrascan camera) were acquired using a TECNAI F20 Transmission Electron Microscope (FEI)

1328   with a field emission gun (FEG) as an electron source, operated at 200kV. The SerialEM

1329   software(Mastronarde and Held, 2017; Schorb et al., 2019) was used for multi-scale mapping as

1330   previously described(Cretin et al., 2021). The 'Align Serial Sections/Blend Montages' interface of

1331   IMOD16 was used for blending the stacks of micrographs collected to single large images.

46

1332　Quantification of mitochondrial cross- sectional area was determined by tracing the perimeter of

1333　individual mitochondria with the use of 3dmod software.

1334

1335　**Primary adult cardiomyocytes isolation**

1336　Primary adult ventricular cardiomyocytes (CMs) were isolated from WT (*Myh6-Cre*^{+/+}, *Mtfp1*[LoxP/LoxP])

1337　and *Mtfp1* KO mice (cMKO, *Myh6-Cre*[Tg/+], *Mtfp1*[LoxP/LoxP]) mice aged 8-10 weeks to perform live-

1338　cell imaging experiments by using the simplified Langendorff-free method as previously published

1339　(Ackers-Johnson et al., 2016) with some modifications**.** Briefly, mice were weighed, injected

1340　intraperitoneally with ketamine/xylazine (ketamine: 3 x 80 mg/kg/bw; xylazine 3 x 10 mg/kg/bw).

1341　Once the thorax was opened, the descending aorta was cut and the heart exposed and flushed

1342　into the right ventricle with EDTA buffer pH 7.8 (NaCl 130 mM, KCl 5 mM, NaH_2PO_4 0.5 mM,

1343　HEPES 10 mM, Glucose 10 mM, 2,3-butanedione monoxime (BDM) 10 mM, Taurine 10 mM,

1344　EDTA 5 mM). The heart was then excised, transferred into a dish containing EDTA buffer, where

1345　the ascending aorta was clamped. Tissue digestion was performed by sequential injection of EDTA

1346　buffer, perfusion buffer (NaCl 130 mM, KCl 5 mM, NaH_2PO_4 0.5 mM, HEPES 10 mM, Glucose 10

1347　mM, BDM 10 mM, Taurine 10 mM, MgCl2 1 mM, pH 7.8) and collagenase buffer (Collagenase II

1348　0.5 mg/mL, Collagenase 4 0.5 mg/mL, Protease XIV 0.05 mg/mL) into the left ventricle (LV)

1349　through the apex. To control the flow of the digestion buffer the LV was perfused via a flexible

1350　linker using an automated infusion pump (Graseby 3200). After digestion, ventricles were then

1351　separated from the atria and ultimately dissociated by gentle pipetting. The digestion process was

1352　then inhibited by the addition of the stop buffer (perfusion buffer containing FBS 10%). Cellular

1353　suspension was filtered using a 100 µm pore size strainer to remove undigested debris. CMs were

1354　then collected by gravity settling (15 min) while resuspended sequentially in 3 calcium

1355　reintroduction buffers to gradually restore calcium levels (0.34 mM, 0.68 mM, and 1.02 mM Ca^{2+}).

1356　CMs yields were quantified using a hemocytometer. CMs were resuspended in prewarmed culture

1357　media (M199 Medium, BSA 0.1%, Insulin-Transferrin-Selenium (ITS) 1x, BDM 10 mmol/l, CD lipid

1358　1x, P/S 1x), and plated into laminin (10 µg/mL) precoated Cell Carrier Ultra-96 well (Perkin Elmer)

1359　plates, in a humidified tissue culture incubator (37°C, 5% CO_2) for at least 1 hour before

1360　proceeding to live imaging.

1361

Cell death assay

CMs isolated from WT and cMKO mice (8-10 weeks) labelled with NucBlue™ Live ReadyProbes™ Reagent (ThermoFisher Scientific) and Tetramethylrhodamine Ethyl Ester Perchlorate (TMRE; 50 nM) for 20 min at 37°C, 5% CO_2. Supervised machine learning (Harmony 4.9, Perkin Elmer) using TMRE intensity, cell geometry (rod- shape, area, length) and nuclei number as read-outs enabled the on-the-fly detection, imaging, and quantification of healthy CMs from dead and dying CMs and non-myocytes. Live-cell imaging was performed in the presence or absence of a cell death stimuli: H_2O_2 (25 µM), or doxorubicin (Doxo, 60 µM,) or carbonyl cyanide m-chlorophenyl hydrazine (CCCP, 10 µM). Image acquisition was performed using the Operetta CLS High-Content Analysis system (Perkin Elmer) with a 5x air objective.

WT, *Mtfp1*$^{-/-}$, *Ppif*$^{-/-}$ and *Mtfp1*$^{-/-}$*Ppif*$^{-/-}$ MEFs were plated in Cell Carrier Ultra-96 well (Perkin Elmer) and incubated 24h with regular media. Cells were then stained with NucBlue™ Live ReadyProbes™ to visualize nuclei. CellEvent Caspase 3/7 Green (CE) was added (1 drop per 1 mL of media) to visualize the activation of caspases 3/7 in cells undergoing to apoptosis. Propidium Iodide (PI, 1:500) was added to visualize dead cells. Cell death was induced with actinomycin D (1.5 µM) alone, or in association with ABT-737 (10 µM)**,** an inhibitor of the Bcl-2 family proteins, or doxorubicin hydrochloride (DOXO, 1.5 µM), or staurosporine (1 µM) or hydrogen peroxide H_2O_2 (500 µM). The pan-caspase inhibitor Q-VD-OPh (qVD, 20 µM**)** and cyclophilin D inhibitor cyclosporin A (CsA, 2 µM), were added where indicated. Image acquisition was performed using the Operetta CLS High-Content Analysis system (Perkin Elmer) with a 20x air objective. CE or PI positive nuclei number were automatically counted by using Harmony 4.9 software.

Field-stimulated cardiomyocytes

Adult ventricular cardiomyocytes (CMs) from WT and cMKO mice (8-10 weeks) were isolated with a Langendorff system as previously described (Chen et al., 2012; Nickel et al., 2015) and paced by electrical field stimulation at 37°C using a customized IonOptix system. CMs were exposed to a protocol that simulates a physiological workload increase by first pacing cells at 0.5 Hz in Normal Tyrode´s solution pH 7.4 [NT; NaCl 130 mM, KCl 5 mM, $MgCl_2$ 1 mM, $CaCl_2$ 1 mM, Na-HEPES 10 mM, glucose 10 mM, sodium pyruvate 2 mM and ascorbic acid 0.3 mM]. The β-adrenergic receptor agonist isoproterenol (30 nM) was then washed in for 1 min and then the stimulation rate was

48

1392 increased to 5 Hz for 3 min. After this time, stimulation rate was set back to the initial 0.5 Hz, and

1393 isoproterenol washed out. During the measurements or sarcomere length and contraction, the

1394 system detection was combined to recordings of the autofluorescence of NAD(P)H/NAD(P)$^+$ and

1395 FADH$_2$/FAD by alternately exciting cells at wavelengths (λ_{exc}) of 340 and 485 nm and collecting

1396 emission (λ_{em}) at 450 and 525 nm for NAD(P)H and FAD$^+$, respectively. Calibration was performed

1397 inducing maximal oxidation and reduction of NAD(P)H/FADH2 with FCCP (5 µmol/L) and cyanide

1398 (4 mmol/L), respectively.

1399

1400 **Intracellular Calcium measurement**

1401 LV cardiac myocytes were isolated by enzymatic digestion and were paced by electrical field

1402 stimulation at 37°C using a customized IonOptix system as described previously(Kohlhaas and

1403 Maack, 2010; Kohlhaas et al., 2010). [Ca^{2+}]$_C$ was measured by incubating cells with indo-1 AM (5

1404 µmol/L) for 20 min at 25°C (λexc=340 nm, λem=405/485 nm). The bath solution contains (mM):

1405 130 NaCL; 5 KCl; 1 MgCL2; 10 sodium HEPES; 2 sodium pyruvate; 0.3 ascorbic acid; 10 glucose

1406 and was adjust at pH 7.4 at 37°C; Isoproterenol was used at 3×10^{-8} M. The Ca^{2+} transients were

1407 analysed with the IONWIZRD software from IONOptix. Data were collected and statistically

1408 analysed using paired or unpaired tTest or 2way ANOVA & Bonferroni´s Multiple Comparison Test.

1409

1410 **Mitochondrial swelling and mPTP opening**

1411 Calcium-induced mitochondrial permeability transition pore (mPTP) opening was determined in

1412 freshly isolated cardiac mitochondria from WT and cMKO mice aged 8-10 weeks as previously

1413 described (Palmeira CM, 2018) . Mitochondria were suspended in Ca^{2+} uptake buffer pH 7.4 (120

1414 mM KCl, 5 mM MOPS, 5 mM KH$_2$PO$_4$, 10 mM Glutamate, 5 mM Malate *plus* cOmplete™, EDTA-

1415 free Protease Inhibitor Cocktail (Roche) at a concentration of 0.5 mg/mL and stimulated by the

1416 addition of a single pulse of 120 µM CaCl$_2$.

1417 mPTP opening was assessed in mitochondria of WT, *Mtfp1$^{-/-}$*, *Ppif$^{/-}$* and *Mtfp1$^{-/-}$Ppif$^{/-}$* MEFs as

1418 previously described (Karch et al., 2013) at a concentration of 1 mg/mL in mitochondrial swelling

1419 buffer (120 mM KCl, 10 mM Tris pH 7.4, 5 mM KH$_2$PO$_4$, 7 mM pyruvate, 1 mM malate, and 10 µM

1420 EDTA). Swelling was induced by pulsing mitochondria with 250 µM CaCl$_2$ in EDTA-free buffer.

1421 The absorbance (540 nm) was measured at intervals of ~20 seconds at 37°C using the microplate

1422 reader Infinite® M Plex (Tecan). Cyclosporin A (CsA, 1 µM Sigma) was used as a control to inhibit

1423 mPTP-dependent mitochondrial swelling.

1424

1425 **BN-PAGE of cardiac mitochondria**

1426 BN-PAGE was performed as described previously (Wittig et al., 2006) with some modifications.

1427 Briefly, cardiac mitochondria were isolated from WT and cMKO mice at 8-10 weeks and solubilized

1428 with sample buffer (30 mM HEPES, 150 mM Potassium Acetate, 12% glycerol, 2 mM acid 6-

1429 aminohexanoic, 1 mM disodium EDTA) containing digitonin 6% (w/w). Lysates were incubated for

1430 1h at 4°C and then centrifuged at 30,000 g for 20 minutes. Supernatants were then mixed with

1431 G250 sample additive 1% (Invitrogen, BN2004) and resolved on 3-12% Bis-Tris Gels (1.0 mm)

1432 (Invitrogen, BN2011BX10) using the anode running buffer (Invitrogen, BN2001) and Cathode

1433 Buffer Additive added to the anode buffer (InVitroGen, BN2002). Gels were then subjected to a

1434 semi-dry transfer using PVDF membranes (GE, 10600023). Membranes were washed with

1435 methanol and then blocked for at least 1h with 5% (w/v) semi-skimmed dry milk dissolved in Tris-

1436 buffered saline Tween 0.1% (TBST), incubated overnight at 4°C with primary antibodies dissolved

1437 1:1.000 in 2% (w/v) Bovine Serum Albumin (BSA), 0.1% TBST. The next day membranes were

1438 incubated in secondary antibodies conjugated to horseradish peroxidase (HRP) at room

1439 temperature for 2h (diluted 1:10,000 in BSA 2% TBST 0.1%). Finally, membranes were incubated

1440 in Clarity™ Western ECL Substrate (Bio-Rad) for 2 min and luminescence was detected using the

1441 ChemiDoc® Gel Imaging System. Primary antibodies are listed in Dataset EV4.

1442

1443 **Co-Immunoprecipitation assay**

1444 500 µg of cardiac crude mitochondria were freshly isolated from heart tissue of cardiomyocyte

1445 specific Flag-MTFP1 Knock-In (KI) mice (*Myh6-Cre$^{tg/+}$Mtfp1$^{+/+}$, CAG$^{tg+/}$*) and WT mice (*Myh6-*

1446 *Cre$^{+/+}$Mtfp1$^{+/+}$, CAG$^{tg+/}$*) as described above. Mitochondria were lysed in IP buffer (20 mM HEPES-

1447 KOH pH 7.5, 150 mM NaCl, 0.25% Triton X-100, protease inhibitor cocktail) on ice for 20 min and

1448 then centrifugated at 10000 g, 4°C for 15 min. Supernatant obtained by centrifugation was then

1449 incubated with 20 µL of anti-FLAG magnetic beads (Sigma M8823) for 2 hours at 4°C. The

1450 immunocomplexes were then washed with IP buffer without Triton X-100 and eluted with Laemmli

50

1451 Sample Buffer 2x at 95°C for 5 min. Protein were stacked in a 15 % SDS-PAGE gel with a 10 min

1452 long migration at 80 V. Proteins were fixed in gel and migration was visualized using the Instant

1453 Blue stain (Expedeon). Bands were excised for digestion. Gel bands were washed twice in

1454 Ammonium bicarbonate (AmBi) 50 mM, once with AmBi 50 mM / ACN 50 % and once with 100%

1455 ANC. Gel band were incubated for 30 min at 56°C in 5 mM dithiothreitol (DTT) solution for

1456 reduction. Gel bands were washed in AmBi 50 mM and then in 100% ACN. Alkylation was

1457 performed at room temp in the dark by incubation of the gel bands in Iodocateamide 55 mM

1458 solution. Gel bands were washed twice in AmBi 50mM and in 100% ACN. 600 ng of trypsin were

1459 added for a 8h digestion at 37°C. Peptides were extracted by collecting 3 washes of the gel bands

1460 using AmBi 50 mM / 50 % ACN and 5 % FA. Peptides clean up and desalting was done using

1461 Stage tips (2 disc Empore C18 discs stacked in a P200 tip).

1462 LC-MS/SM analysis of digested peptides was performed on an Orbitrap Q Exactive HF mass

1463 spectrometer (Thermo Fisher Scientific, Bremen) coupled to an EASY-nLC 1200 (Thermo Fisher

1464 Scientific). A home-made column was used for peptide separation (C_{18} 30 cm capillary column

1465 picotip silica emitter tip (75 μm diameter filled with 1.9 μm Reprosil-Pur Basic C_{18}-HD resin, (Dr.

1466 Maisch GmbH, Ammerbuch-Entringen, Germany)). It was equilibrated and peptide were loaded in

1467 solvent A (0.1 % FA) at 900 bars. Peptides were separated at 250 nl.min^{-1}. Peptides were eluted

1468 using a gradient of solvent B (ACN, 0.1 % FA) from 3% to 26% in 105 min, 26% to 48% in 20 min

1469 (total length of the chromatographic run was 145 min including high ACN level step and column

1470 regeneration). Mass spectra were acquired in data-dependent acquisition mode with the XCalibur

1471 2.2 software (Thermo Fisher Scientific, Bremen) with automatic switching between MS and MS/MS

1472 scans using a top 12 method. MS spectra were acquired at a resolution of 60000 (at m/z 400) with

1473 a target value of 3×10^6 ions. The scan range was limited from 400 to 1700 m/z. Peptide

1474 fragmentation was performed using HCD with the energy set at 26 NCE. Intensity threshold for

1475 ions selection was set at 1×10^5 ions with charge exclusion of z = 1 and z > 7. The MS/MS spectra

1476 were acquired at a resolution of 15000 (at m/z 400). Isolation window was set at 1.6 Th. Dynamic

1477 exclusion was employed within 30 s.

1478 <u>Data Processing</u>

1479 Data were searched using MaxQuant (version 1.6.6.0) [1,2] using the Andromeda search engine

1480 [3] against a reference proteome of Mus musculus (53449 entries, downloaded from Uniprot the

51

1481   24th of July 2018). A modified sequence of the protein MTP18 with a Flag tag in its N-ter part was

1482   also searched.

1483   The following search parameters were applied: carbamidomethylation of cysteines was set as a

1484   fixed modification, oxidation of methionine and protein N-terminal acetylation were set as variable

1485   modifications. The mass tolerances in MS and MS/MS were set to 5 ppm and 20 ppm respectively.

1486   Maximum peptide charge was set to 7 and 5 amino acids were required as minimum peptide

1487   length. A false discovery rate of 1% was set up for both protein and peptide levels. The iBAQ

1488   intensity was used to estimate the protein abundance within a sample. The match between runs

1489   features was allowed for biological replicate only.

1490   For this Affinity Purification Mass Spectrometry analysis part, the mass spectrometry data have

1491   been deposited at the ProteomeXchange Consortium (http://www.proteomexchange.org) via the

1492   PRIDE partner repository(Perez-Riverol et al., 2019; Vizcaíno et al., 2014) with the dataset

1493   identifier PXD028529

1494   <u>Data analysis</u>

1495   Quantitative analysis was based on pairwise comparison of intensities. Values were log-

1496   transformed (log2). Reverse hits and potential contaminant were removed from the analysis.

1497   Proteins with at least 2 peptides (including one unique peptide) were kept for further statistics.

1498   Intensities values were normalized by median centering within conditions (normalizeD function of

1499   the R package DAPAR). Remaining proteins without any iBAQ value in one of both conditions

1500   have been considered as proteins quantitatively present in a condition and absent in the other.

1501   They have therefore been set aside and considered as differentially abundant proteins. Next,

1502   missing values were imputed using the impute.MLE function of the R package imp4p. Statistical

1503   testing was conducted using a limma t-test thanks to the R package limma(Pounds and Cheng,

1504   2006). An adaptive Benjamini-Hochberg procedure was applied on the resulting p-values thanks to

1505   the function adjust.p of R package cp4p(Smyth, 2004) using the robust method previously

1506   described(Giai Gianetto et al., 2016) to estimate the proportion of true null hypotheses among the

1507   set of statistical tests. The proteins associated to an adjusted p-value inferior to a FDR level of 1%

1508   have been considered as significantly differentially abundant proteins.

1509   **Statistical Analyses**

1510 Experiments were repeated at least three times and quantitative analyses were conducted blindly.

1511 Randomization of groups (e.g., different genotypes) was performed when simultaneous, parallel

1512 measurements were not performed (e.g., Oroboros, CM isolation). For high-throughput

1513 measurements (e.g., mitochondrial morphology, cell death), all groups were measured in parallel

1514 to reduce experimental bias. Statistical analyses were performed using GraphPad Prism 9

1515 software. Data are presented as mean ± SD or SEM where indicated. The statistical tests used,

1516 and value of experiment replicates are described in the figure legends. Comparisons between two

1517 groups were performed by unpaired two-tailed T test. To compare more than two groups or groups

1518 at multiple time points 1-way ANOVA or 2-way ANOVA was applied. Tests were considered

1519 significant at p-value < 0.05 (*p< 0.05; **p< 0.01; ***p < 0.001; ****p< 0.0001).

1520

1534

1535

References

Acin-Perez, R., Lechuga-Vieco, A.V., Muñoz, M. del M., Nieto-Arellano, R., Torroja, C., Sánchez-Cabo, F., Jiménez, C., González-Guerra, A., Carrascoso, I., Benincá, C., et al. (2018). Ablation of the stress protease OMA1 protects against heart failure in mice. Science Translational Medicine *10*.

Ackers-Johnson, M., Li, P.Y., and Holmes, A.P. (2016). A Simplified, Langendorff-Free Method for Concomitant Isolation of Viable Cardiac Myocytes and Non-Myocytes from the Adult Mouse Heart. Circulation.

Adams, S.H. (2000). Uncoupling protein homologs: emerging views of physiological function. J. Nutr. *130*, 711–714.

Agah, R., Frenkel, P.A., French, B.A., Michael, L.H., Overbeek, P.A., and Schneider, M.D. (1997). Gene recombination in postmitotic cells. Targeted expression of Cre recombinase provokes cardiac-restricted, site-specific rearrangement in adult ventricular muscle in vivo. J. Clin. Invest. *100*, 169–179.

Anand, R., Wai, T., Baker, M.J., Kladt, N., Schauss, A.C., Rugarli, E., and Langer, T. (2014). The i-AAA protease YME1L and OMA1 cleave OPA1 to balance mitochondrial fusion and fission. The Journal of Cell Biology *204*, 919–929.

Antonicka, H., Leary, S.C., Guercin, G.-H., Agar, J.N., Horvath, R., Kennaway, N.G., Harding, C.O., Jaksch, M., and Shoubridge, E.A. (2003a). Mutations in COX10 result in a defect in mitochondrial heme A biosynthesis and account for multiple, early-onset clinical phenotypes associated with isolated COX deficiency. Hum. Mol. Genet. *12*, 2693–2702.

Antonicka, H., Mattman, A., Carlson, C.G., Glerum, D.M., Hoffbuhr, K.C., Leary, S.C., Kennaway, N.G., and Shoubridge, E.A. (2003b). Mutations in COX15 Produce a Defect in the Mitochondrial Heme Biosynthetic Pathway, Causing Early-Onset Fatal Hypertrophic Cardiomyopathy. The American Journal of Human Genetics *72*, 101–114.

Ashrafian, H., Docherty, L., Leo, V., Towlson, C., Neilan, M., Steeples, V., Lygate, C.A., Hough, T., Townsend, S., Williams, D., et al. (2010). A Mutation in the Mitochondrial Fission Gene Dnm1l Leads to Cardiomyopathy. PLOS Genetics *6*, e1001000.

Aung, L.H.H., Li, R., Prabhakar, B.S., and Li, P. (2017a). Knockdown of Mtfp1 can minimize doxorubicin cardiotoxicity by inhibiting Dnm1l-mediated mitochondrial fission. Journal of Cellular and Molecular Medicine *21*, 3394–3404.

Aung, L.H.H., Li, R., Prabhakar, B.S., Maker, A.V., and Li, P. (2017b). Mitochondrial protein 18 (MTP18) plays a pro-apoptotic role in chemotherapy-induced gastric cancer cell apoptosis. Oncotarget.

Aung, L.H.H., Li, Y.-Z., Yu, H., Chen, X., Yu, Z., Gao, J., and Li, P. (2019). Mitochondrial protein 18 is a positive apoptotic regulator in cardiomyocytes under oxidative stress. Clin. Sci. *133*, 1067–1084.

Baines, C.P., Kaiser, R.A., Purcell, N.H., Blair, N.S., Osinska, H., Hambleton, M.A., Brunskill, E.W., Sayen, M.R., Gottlieb, R.A., Dorn, G.W., et al. (2005). Loss of cyclophilin D reveals a critical role for mitochondrial permeability transition in cell death. Nature *434*, 658–662.

Basso, E., Petronilli, V., Forte, M.A., and Bernardi, P. (2008). Phosphate is essential for inhibition of the mitochondrial permeability transition pore by cyclosporin A and by cyclophilin D ablation. J. Biol. Chem. *283*, 26307–26311.

Bernardi, P., Rasola, A., Forte, M., and Lippe, G. (2015). The Mitochondrial Permeability Transition Pore: Channel Formation by F-ATP Synthase, Integration in Signal Transduction, and Role in Pathophysiology. Physiol. Rev. *95*, 1111–1155.

1582 Bertero, E., Nickel, A., Kohlhaas, M., Hohl, M., Sequeira, V., Brune, C., Schwemmlein, J., Abeßer,
1583 M., Schuh, K., Kutschka, I., et al. Loss of Mitochondrial Ca2+ Uniporter Limits Inotropic Reserve
1584 and Provides Trigger and Substrate for Arrhythmias in Barth Syndrome Cardiomyopathy.
1585 Circulation *0*.

1586 Bertholet, A.M., Chouchani, E.T., Kazak, L., Angelin, A., Fedorenko, A., Long, J.Z., Vidoni, S.,
1587 Garrity, R., Cho, J., Terada, N., et al. (2019). H+ transport is an integral function of the
1588 mitochondrial ADP/ATP carrier. Nature *571*, 515–520.

1589 Bock, F.J., and Tait, S.W.G. (2020). Mitochondria as multifaceted regulators of cell death. Nature
1590 Reviews Molecular Cell Biology *21*, 85–100.

1591 Brand, M.D., Affourtit, C., Esteves, T.C., Green, K., Lambert, A.J., Miwa, S., Pakay, J.L., and
1592 Parker, N. (2004). Mitochondrial superoxide: production, biological effects, and activation of
1593 uncoupling proteins. Free Radic. Biol. Med. *37*, 755–767.

1594 Brand, M.D., Pakay, J.L., Ocloo, A., Kokoszka, J., Wallace, D.C., Brookes, P.S., and Cornwall, E.J.
1595 (2005). The basal proton conductance of mitochondria depends on adenine nucleotide translocase
1596 content. Biochemical Journal *392*, 353–362.

1597 Burke, M.A., Chang, S., Wakimoto, H., Gorham, J.M., Conner, D.A., Christodoulou, D.C.,
1598 Parfenov, M.G., DePalma, S.R., Eminaga, S., Konno, T., et al. (2016). Molecular profiling of dilated
1599 cardiomyopathy that progresses to heart failure. JCI Insight *1*.

1600 Carraro, M., Checchetto, V., Sartori, G., Kucharczyk, R., di Rago, J.-P., Minervini, G., Franchin, C.,
1601 Arrigoni, G., Giorgio, V., Petronilli, V., et al. (2018). High-Conductance Channel Formation in Yeast
1602 Mitochondria is Mediated by F-ATP Synthase e and g Subunits. Cell. Physiol. Biochem. *50*, 1840–
1603 1855.

1604 Carraro, M., Carrer, A., Urbani, A., and Bernardi, P. (2020). Molecular nature and regulation of the
1605 mitochondrial permeability transition pore(s), drug target(s) in cardioprotection. Journal of
1606 Molecular and Cellular Cardiology *144*, 76–86.

1607 Chance, B., and Williams, G.R. (1956). The Respiratory Chain and Oxidative Phosphorylation. In
1608 Advances in Enzymology and Related Areas of Molecular Biology, (John Wiley & Sons, Ltd), pp.
1609 65–134.

1610 Chen, E.Y., Tan, C.M., Kou, Y., Duan, Q., Wang, Z., Meirelles, G.V., Clark, N.R., and Ma'ayan, A.
1611 (2013). Enrichr: interactive and collaborative HTML5 gene list enrichment analysis tool. BMC
1612 Bioinformatics *14*, 128.

1613 Chen, H., Ren, S., Clish, C., Jain, M., Mootha, V., McCaffery, J.M., and Chan, D.C. (2015).
1614 Titration of mitochondrial fusion rescues Mff-deficient cardiomyopathy. J. Cell Biol. *211*, 795–805.

1615 Chen, L., Gong, Q., Stice, J.P., and Knowlton, A.A. (2009). Mitochondrial OPA1, apoptosis, and
1616 heart failure. Cardiovascular Research *84*, 91–99.

1617 Chen, Y., Csordás, G., Jowdy, C., Schneider, T.G., Csordás, N., Wang, W., Liu, Y., Kohlhaas, M.,
1618 Meiser, M., Bergem, S., et al. (2012). Mitofusin 2-containing mitochondrial-reticular microdomains
1619 direct rapid cardiomyocyte bioenergetic responses via interorganelle Ca(2+) crosstalk. Circ. Res.
1620 *111*, 863–875.

1621 Chiao, Y.A., Zhang, H., Sweetwyne, M., Whitson, J., Ting, Y.S., Basisty, N., Pino, L.K., Quarles,
1622 E., Nguyen, N.-H., Campbell, M.D., et al. (2020). Late-life restoration of mitochondrial function
1623 reverses cardiac dysfunction in old mice. ELife *9*, e55513.

1624 Cho, B., Cho, H.M., Jo, Y., Kim, H.D., Song, M., Moon, C., Kim, H., Kim, K., Sesaki, H., Rhyu, I.J.,
1625 et al. (2017). Constriction of the mitochondrial inner compartment is a priming event for
1626 mitochondrial division. Nature Communications *8*, 15754.

1627 Christidi, E., and Brunham, L.R. (2021). Regulated cell death pathways in doxorubicin-induced
1628 cardiotoxicity. Cell Death Dis *12*, 1–15.

1629 Cokelaer, T., Desvillechabrol, D., Legendre, R., and Cardon, M. (2017). "Sequana": a Set of
1630 Snakemake NGS pipelines. JOSS *2*, 352.

1631 Cortassa, S., Aon, M.A., Marbán, E., Winslow, R.L., and O'Rourke, B. (2003). An Integrated Model
1632 of Cardiac Mitochondrial Energy Metabolism and Calcium Dynamics. Biophysical Journal *84*,
1633 2734–2755.

1634 Cretin, E., Lopes, P., Vimont, E., Tatsuta, T., Langer, T., Gazi, A., Sachse, M., Yu-Wai-Man, P.,
1635 Reynier, P., and Wai, T. (2021). High-throughput screening identifies suppressors of mitochondrial
1636 fragmentation in OPA1 fibroblasts. EMBO Molecular Medicine *n/a*, e13579.

1637 Dobin, A., Davis, C.A., Schlesinger, F., Drenkow, J., Zaleski, C., Jha, S., Batut, P., Chaisson, M.,
1638 and Gingeras, T.R. (2013). STAR: ultrafast universal RNA-seq aligner. Bioinformatics *29*, 15–21.

1639 Duroux-Richard, I., Roubert, C., Ammari, M., Présumey, J., Grün, J.R., Häupl, T., Grützkau, A.,
1640 Lecellier, C.-H., Boitez, V., Codogno, P., et al. (2016). miR-125b controls monocyte adaptation to
1641 inflammation through mitochondrial metabolism and dynamics. Blood *128*, 3125–3136.

1642 Echtay, K.S., Roussel, D., St-Pierre, J., Jekabsons, M.B., Cadenas, S., Stuart, J.A., Harper, J.A.,
1643 Roebuck, S.J., Morrison, A., Pickering, S., et al. (2002). Superoxide activates mitochondrial
1644 uncoupling proteins. Nature *415*, 96–99.

1645 Ewels, P., Magnusson, M., Lundin, S., and Käller, M. (2016). MultiQC: summarize analysis results
1646 for multiple tools and samples in a single report. Bioinformatics *32*, 3047–3048.

1647 Fernandez-Caggiano, M., Kamynina, A., Francois, A.A., Prysyazhna, O., Eykyn, T.R., Krasemann,
1648 S., Crespo-Leiro, M.G., Vieites, M.G., Bianchi, K., Morales, V., et al. (2020). Mitochondrial pyruvate
1649 carrier abundance mediates pathological cardiac hypertrophy. Nat Metab *2*, 1223–1231.

1650 Fonseca, T.B., Sánchez-Guerrero, Á., Milosevic, I., and Raimundo, N. (2019). Mitochondrial fission
1651 requires DRP1 but not dynamins. Nature *570*, E34–E42.

1652 Ghazal, N., Peoples, J.N., Mohiuddin, T.A., and Kwong, J.Q. (2021). Mitochondrial functional
1653 resilience after TFAM ablation in the adult heart. Am. J. Physiol. Cell Physiol.

1654 Giacomello, M., Pyakurel, A., Glytsou, C., and Scorrano, L. (2020). The cell biology of
1655 mitochondrial membrane dynamics. Nature Reviews Molecular Cell Biology.

1656 Giai Gianetto, Q., Combes, F., Ramus, C., Bruley, C., Couté, Y., and Burger, T. (2016). Calibration
1657 plot for proteomics: A graphical tool to visually check the assumptions underlying FDR control in
1658 quantitative experiments. PROTEOMICS *16*, 29–32.

1659 Graham, B.H., Waymire, K.G., Cottrell, B., Trounce, I.A., MacGregor, G.R., and Wallace, D.C.
1660 (1997). A mouse model for mitochondrial myopathy and cardiomyopathy resulting from a
1661 deficiency in the heart/muscle isoform of the adenine nucleotide translocator. Nat Genet *16*, 226–
1662 234.

1663 Halestrap, A.P., and Davidson, A.M. (1990). Inhibition of Ca2+-induced large-amplitude swelling of
1664 liver and heart mitochondria by cyclosporin is probably caused by the inhibitor binding to
1665 mitochondrial-matrix peptidyl-prolyl cis-trans isomerase and preventing it interacting with the
1666 adenine nucleotide translocase. Biochemical Journal *268*, 153–160.

1667 Hansson, A., Hance, N., Dufour, E., Rantanen, A., Hultenby, K., Clayton, D.A., Wibom, R., and
1668 Larsson, N.-G. (2004). A switch in metabolism precedes increased mitochondrial biogenesis in
1669 respiratory chain-deficient mouse hearts. Proc. Natl. Acad. Sci. U. S. A. *101*, 3136–3141.

Heide, H., Bleier, L., Steger, M., Ackermann, J., Dröse, S., Schwamb, B., Zörnig, M., Reichert, A.S., Koch, I., Wittig, I., et al. (2012). Complexome profiling identifies TMEM126B as a component of the mitochondrial complex I assembly complex. Cell Metab. *16*, 538–549.

Hohl, M., Wagner, M., Reil, J.-C., Müller, S.-A., Tauchnitz, M., Zimmer, A.M., Lehmann, L.H., Thiel, G., Böhm, M., Backs, J., et al. (2013). HDAC4 controls histone methylation in response to elevated cardiac load. J Clin Invest *123*, 1359–1370.

Houweling, A.C., van Borren, M.M., Moorman, A.F.M., and Christoffels, V.M. (2005). Expression and regulation of the atrial natriuretic factor encoding gene Nppa during development and disease. Cardiovasc Res *67*, 583–593.

Kageyama, Y., Hoshijima, M., Seo, K., Bedja, D., Sysa-Shah, P., Andrabi, S.A., Chen, W., Höke, A., Dawson, V.L., Dawson, T.M., et al. (2014). Parkin-independent mitophagy requires Drp1 and maintains the integrity of mammalian heart and brain. The EMBO Journal *33*, 2798–2813.

Kang, B.H., Plescia, J., Dohi, T., Rosa, J., Doxsey, S.J., and Altieri, D.C. (2007). Regulation of Tumor Cell Mitochondrial Homeostasis by an Organelle-Specific Hsp90 Chaperone Network. Cell *131*, 257–270.

Karamanlidis, G., Lee, C.F., Garcia-Menendez, L., Kolwicz, S.C., Suthammarak, W., Gong, G., Sedensky, M.M., Morgan, P.G., Wang, W., and Tian, R. (2013). Mitochondrial Complex I Deficiency Increases Protein Acetylation and Accelerates Heart Failure. Cell Metabolism *18*, 239–250.

Karch, J., Kwong, J.Q., Burr, A.R., Sargent, M.A., Elrod, J.W., Peixoto, P.M., Martinez-Caballero, S., Osinska, H., Cheng, E.H.-Y., Robbins, J., et al. (2013). Bax and Bak function as the outer membrane component of the mitochondrial permeability pore in regulating necrotic cell death in mice. Elife *2*, e00772.

Karch, J., Bround, M.J., Khalil, H., Sargent, M.A., Latchman, N., Terada, N., Peixoto, P.M., and Molkentin, J.D. (2019). Inhibition of mitochondrial permeability transition by deletion of the ANT family and CypD. Sci Adv *5*, eaaw4597.

Kohlhaas, M., and Maack, C. (2010). Adverse Bioenergetic Consequences of Na+-Ca2+ Exchanger–Mediated Ca2+ Influx in Cardiac Myocytes. Circulation *122*, 2273–2280.

Kohlhaas, M., Liu, T., Knopp, A., Zeller, T., Ong, M.F., Böhm, M., O'Rourke, B., and Maack, C. (2010). Elevated Cytosolic Na+ Increases Mitochondrial Formation of Reactive Oxygen Species in Failing Cardiac Myocytes. Circulation *121*, 1606–1613.

Kohlhaas, M., Nickel, A.G., and Maack, C. (2017). Mitochondrial energetics and calcium coupling in the heart. The Journal of Physiology *595*, 3753–3763.

Kolwicz, S.C., Jr, Purohit, S., and Tian, R. (2013). Cardiac metabolism and its interactions with contraction, growth, and survival of cardiomyocytes. Circ. Res. *113*, 603–616.

Köster, J., and Rahmann, S. (2012). Snakemake—a scalable bioinformatics workflow engine. Bioinformatics *28*, 2520–2522.

Kulak, N.A., Pichler, G., Paron, I., Nagaraj, N., and Mann, M. (2014). Minimal, encapsulated proteomic-sample processing applied to copy-number estimation in eukaryotic cells. Nat Methods *11*, 319–324.

Kwong, J.Q., and Molkentin, J.D. (2015). Physiological and Pathological Roles of the Mitochondrial Permeability Transition Pore in the Heart. Cell Metabolism *21*, 206–214.

Kwong, J.Q., Davis, J., Baines, C.P., Sargent, M.A., Karch, J., Wang, X., Huang, T., and Molkentin, J.D. (2014). Genetic deletion of the mitochondrial phosphate carrier desensitizes the mitochondrial permeability transition pore and causes cardiomyopathy. Cell Death Differ. *21*, 1209–1217.

Lei, Y., Guerra Martinez, C., Torres-Odio, S., Bell, S.L., Birdwell, C.E., Bryant, J.D., Tong, C.W., Watson, R.O., West, L.C., and West, A.P. (2021). Elevated type I interferon responses potentiate metabolic dysfunction, inflammation, and accelerated aging in mtDNA mutator mice. Sci. Adv. *7*, eabe7548.

Lewis, S.C., Uchiyama, L.F., and Nunnari, J. (2016). ER-mitochondria contacts couple mtDNA synthesis with mitochondrial division in human cells. Science *353*, aaf5549–aaf5549.

Liao, X., Zhang, R., Lu, Y., Prosdocimo, D.A., Sangwung, P., Zhang, L., Zhou, G., Anand, P., Lai, L., Leone, T.C., et al. (2015). Kruppel-like factor 4 is critical for transcriptional control of cardiac mitochondrial homeostasis. J. Clin. Invest. *125*, 3461–3476.

Liao, Y., Smyth, G.K., and Shi, W. (2014). featureCounts: an efficient general purpose program for assigning sequence reads to genomic features. Bioinformatics *30*, 923–930.

Livak, K.J., and Schmittgen, T.D. (2001). Analysis of Relative Gene Expression Data Using Real-Time Quantitative PCR and the 2−ΔΔCT Method. Methods *25*, 402–408.

Losón, O.C., Song, Z., Chen, H., and Chan, D.C. (2013). Fis1, Mff, MiD49, and MiD51 mediate Drp1 recruitment in mitochondrial fission. Mol. Biol. Cell *24*, 659–667.

Lu, J.-H., Shi, Z.-F., and Xu, H. (2014). The mitochondrial cyclophilin D/p53 complexation mediates doxorubicin-induced non-apoptotic death of A549 lung cancer cells. Mol Cell Biochem *389*, 17–24.

Macher, G., Koehler, M., Rupprecht, A., Kreiter, J., Hinterdorfer, P., and Pohl, E.E. (2018). Inhibition of mitochondrial UCP1 and UCP3 by purine nucleotides and phosphate. Biochim. Biophys. Acta Biomembr. *1860*, 664–672.

Martin, M. (2011). Cutadapt removes adapter sequences from high-throughput sequencing reads. EMBnet.Journal *17*, 10–12.

Mastronarde, D.N., and Held, S.R. (2017). Automated tilt series alignment and tomographic reconstruction in IMOD. Journal of Structural Biology *197*, 102–113.

Milduberger, N., Bustos, P.L., González, C., Perrone, A.E., Postan, M., and Bua, J. (2021). Trypanosoma cruzi infection in Cyclophilin D deficient mice. Exp. Parasitol. *220*, 108044.

Mitchell, P. (1961). Coupling of Phosphorylation to Electron and Hydrogen Transfer by a Chemi-Osmotic type of Mechanism. Nature *191*, 144–148.

Mootha, V.K., Arai, A.E., and Balaban, R.S. (1997). Maximum oxidative phosphorylation capacity of the mammalian heart. American Journal of Physiology-Heart and Circulatory Physiology *272*, H769–H775.

Morciano, G., Naumova, N., Koprowski, P., Valente, S., Sardão, V.A., Potes, Y., Rimessi, A., Wieckowski, M.R., and Oliveira, P.J. The mitochondrial permeability transition pore: an evolving concept critical for cell life and death. Biological Reviews *n/a*.

Morita, S.-Y., and Terada, T. (2015). Enzymatic measurement of phosphatidylglycerol and cardiolipin in cultured cells and mitochondria. Sci. Rep. *5*, 11737.

Morita, M., Prudent, J., Basu, K., Goyon, V., Katsumura, S., Hulea, L., Pearl, D., Siddiqui, N., Strack, S., McGuirk, S., et al. (2017). mTOR Controls Mitochondrial Dynamics and Cell Survival via MTFP1. Mol Cell *67*, 922-935.e5.

Mourier, A., Ruzzenente, B., Brandt, T., Kuhlbrandt, W., and Larsson, N.-G. (2014). Loss of LRPPRC causes ATP synthase deficiency. Human Molecular Genetics *23*, 2580–2592.

Nakagawa, T., Shimizu, S., Watanabe, T., Yamaguchi, O., Otsu, K., Yamagata, H., Inohara, H., Kubo, T., and Tsujimoto, Y. (2005). Cyclophilin D-dependent mitochondrial permeability transition regulates some necrotic but not apoptotic cell death. Nature *434*, 652–658.

58

1760 Ng, M.Y.W., Wai, T., and Simonsen, A. (2021). Quality control of the mitochondrion.
1761 Developmental Cell.

1762 Nickel, A.G., von Hardenberg, A., Hohl, M., Löffler, J.R., Kohlhaas, M., Becker, J., Reil, J.-C.,
1763 Kazakov, A., Bonnekoh, J., Stadelmaier, M., et al. (2015). Reversal of Mitochondrial
1764 Transhydrogenase Causes Oxidative Stress in Heart Failure. Cell Metabolism *22*, 472–484.

1765 Osellame, L.D., Singh, A.P., Stroud, D.A., Palmer, C.S., Stojanovski, D., Ramachandran, R., and
1766 Ryan, M.T. (2016). Cooperative and independent roles of the Drp1 adaptors Mff, MiD49 and
1767 MiD51 in mitochondrial fission. J. Cell Sci. *129*, 2170–2181.

1768 Perez-Riverol, Y., Csordas, A., Bai, J., Bernal-Llinares, M., Hewapathirana, S., Kundu, D.J.,
1769 Inuganti, A., Griss, J., Mayer, G., Eisenacher, M., et al. (2019). The PRIDE database and related
1770 tools and resources in 2019: improving support for quantification data. Nucleic Acids Research *47*,
1771 D442–D450.

1772 Pounds, S., and Cheng, C. (2006). Robust estimation of the false discovery rate. Bioinformatics
1773 *22*, 1979–1987.

1774 Rappsilber, J., Mann, M., and Ishihama, Y. (2007). Protocol for micro-purification, enrichment, pre-
1775 fractionation and storage of peptides for proteomics using StageTips. Nat Protoc *2*, 1896–1906.

1776 Rath, S., Sharma, R., Gupta, R., Ast, T., Chan, C., Durham, T.J., Goodman, R.P., Grabarek, Z.,
1777 Haas, M.E., Hung, W.H.W., et al. (2021). MitoCarta3.0: an updated mitochondrial proteome now
1778 with sub-organelle localization and pathway annotations. Nucleic Acids Res. *49*, D1541–D1547.

1779 Reimand, J., Isserlin, R., Voisin, V., Kucera, M., Tannus-Lopes, C., Rostamianfar, A., Wadi, L.,
1780 Meyer, M., Wong, J., Xu, C., et al. (2019). Pathway enrichment analysis and visualization of omics
1781 data using g:Profiler, GSEA, Cytoscape and EnrichmentMap. Nat Protoc *14*, 482–517.

1782 Roesler, A., and Kazak, L. (2020). UCP1-independent thermogenesis. Biochemical Journal *477*,
1783 709–725.

1784 Ruprecht, J.J., and Kunji, E.R.S. (2021). Structural Mechanism of Transport of Mitochondrial
1785 Carriers. Annu. Rev. Biochem. *90*, 535–558.

1786 Schorb, M., Haberbosch, I., Hagen, W.J.H., Schwab, Y., and Mastronarde, D.N. (2019). Software
1787 tools for automated transmission electron microscopy. Nature Methods *16*, 471–477.

1788 Schwanhäusser, B., Busse, D., Li, N., Dittmar, G., Schuchhardt, J., Wolf, J., Chen, W., and
1789 Selbach, M. (2011). Global quantification of mammalian gene expression control. Nature *473*,
1790 337–342.

1791 Schwenk, F., Baron, U., and Rajewsky, K. (1995). A cre -transgenic mouse strain for the
1792 ubiquitous deletion of loxP -flanked gene segments including deletion in germ cells. Nucleic Acids
1793 Research *23*, 5080–5081.

1794 Shirakabe, A., Zhai, P., Ikeda, Y., Saito, T., Maejima, Y., Hsu, C.-P., Nomura, M., Egashira, K.,
1795 Levine, B., and Sadoshima, J. (2016). Drp1-Dependent Mitochondrial Autophagy Plays a
1796 Protective Role Against Pressure Overload-Induced Mitochondrial Dysfunction and Heart Failure.
1797 Circulation *133*, 1249–1263.

1798 Smyth, G.K. (2004). Linear Models and Empirical Bayes Methods for Assessing Differential
1799 Expression in Microarray Experiments. Statistical Applications in Genetics and Molecular Biology
1800 *3*.

1801 Song, M., Mihara, K., Chen, Y., Scorrano, L., and Dorn II, G.W. (2015). Mitochondrial Fission and
1802 Fusion Factors Reciprocally Orchestrate Mitophagic Culling in Mouse Hearts and Cultured
1803 Fibroblasts. Cell Metabolism.

Sprenger, H.-G., and Langer, T. (2019). The Good and the Bad of Mitochondrial Breakups. Trends in Cell Biology *29*, 888–900.

Todisco, S., Di Noia, M.A., Onofrio, A., Parisi, G., Punzi, G., Redavid, G., De Grassi, A., and Pierri, C.L. (2016). Identification of new highly selective inhibitors of the human ADP/ATP carriers by molecular docking and in vitro transport assays. Biochem. Pharmacol. *100*, 112–132.

Tondera, D. (2005). The mitochondrial protein MTP18 contributes to mitochondrial fission in mammalian cells. J Cell Sci *118*, 3049–3059.

Tondera, D., Santel, A., Schwarzer, R., Dames, S., Giese, K., Klippel, A., and Kaufmann, J. (2004). Knockdown of MTP18, a novel phosphatidylinositol 3-kinase-dependent protein, affects mitochondrial morphology and induces apoptosis. J. Biol. Chem. *279*, 31544–31555.

Tondera, D., Grandemange, S., Jourdain, A., Karbowski, M., Mattenberger, Y., Herzig, S., Da Cruz, S., Clerc, P., Raschke, I., Merkwirth, C., et al. (2009). SLP-2 is required for stress-induced mitochondrial hyperfusion. EMBO J. *28*, 1589–1600.

Tyanova, S., Temu, T., and Cox, J. (2016). The MaxQuant computational platform for mass spectrometry-based shotgun proteomics. Nat Protoc *11*, 2301–2319.

Varet, H., Brillet-Guéguen, L., Coppée, J.-Y., and Dillies, M.-A. (2016). SARTools: A DESeq2- and EdgeR-Based R Pipeline for Comprehensive Differential Analysis of RNA-Seq Data. PLOS ONE *11*, e0157022.

Vaseva, A.V., Marchenko, N.D., Ji, K., Tsirka, S.E., Holzmann, S., and Moll, U.M. (2012). p53 Opens the Mitochondrial Permeability Transition Pore to Trigger Necrosis. Cell *149*, 1536–1548.

Vizcaíno, J.A., Deutsch, E.W., Wang, R., Csordas, A., Reisinger, F., Ríos, D., Dianes, J.A., Sun, Z., Farrah, T., Bandeira, N., et al. (2014). ProteomeXchange provides globally coordinated proteomics data submission and dissemination. Nat Biotechnol *32*, 223–226.

Wai, T., and Langer, T. (2016). Mitochondrial Dynamics and Metabolic Regulation. Trends Endocrinol. Metab. *27*, 105–117.

Wai, T., Garcia-Prieto, J., Baker, M.J., Merkwirth, C., Benit, P., Rustin, P., Ruperez, F.J., Barbas, C., Ibanez, B., and Langer, T. (2015). Imbalanced OPA1 processing and mitochondrial fragmentation cause heart failure in mice. Science *350*, aad0116–aad0116.

Wang, K., Gan, T.-Y., Li, N., Liu, C.-Y., Zhou, L.-Y., Gao, J.-N., Chen, C., Yan, K.-W., Ponnusamy, M., Zhang, Y.-H., et al. (2017). Circular RNA mediates cardiomyocyte death via miRNA-dependent upregulation of MTP18 expression. Cell Death Differ. *24*, 1111–1120.

Wittig, I., Braun, H.-P., and Schägger, H. (2006). Blue native PAGE. Nat. Protoc. *1*, 418–428.

Woyda-Ploszczyca, A.M., and Jarmuszkiewicz, W. (2014). Different effects of guanine nucleotides (GDP and GTP) on protein-mediated mitochondrial proton leak. PLoS One *9*, e98969.

Zhang, H., Alder, N.N., Wang, W., Szeto, H., Marcinek, D.J., and Rabinovitch, P.S. (2020a). Reduction of elevated proton leak rejuvenates mitochondria in the aged cardiomyocyte. ELife *9*, e60827.

Zhang, Y., Taufalele, P.V., Cochran, J.D., Robillard-Frayne, I., Marx, J.M., Soto, J., Rauckhorst, A.J., Tayyari, F., Pewa, A.D., Gray, L.R., et al. (2020b). Mitochondrial pyruvate carriers are required for myocardial stress adaptation. Nat Metab *2*, 1248–1264.

Zhou, B., and Tian, R. (2018). Mitochondrial dysfunction in pathophysiology of heart failure. J. Clin. Invest. *128*, 3716–3726.
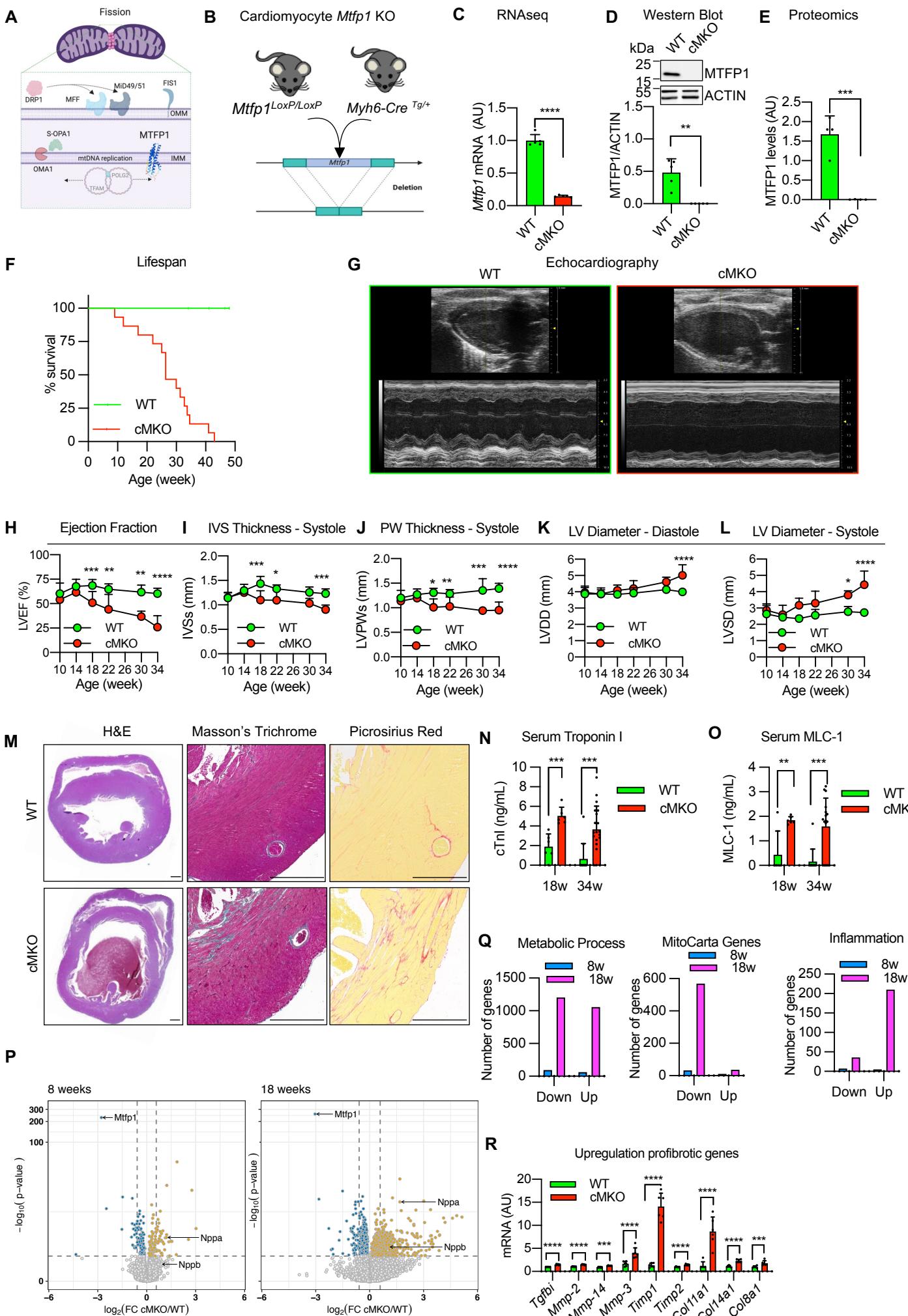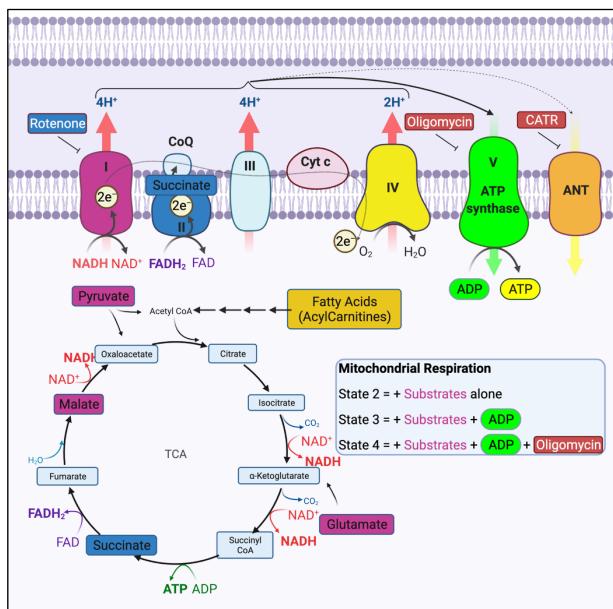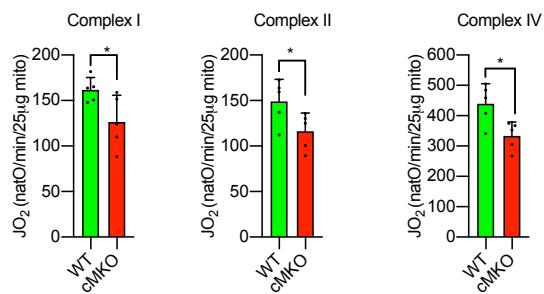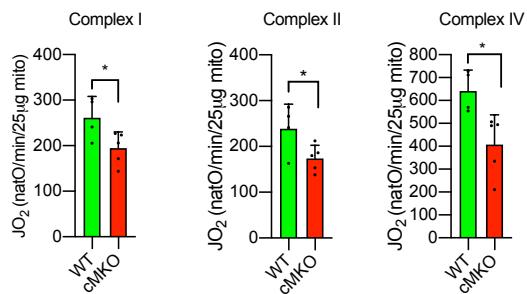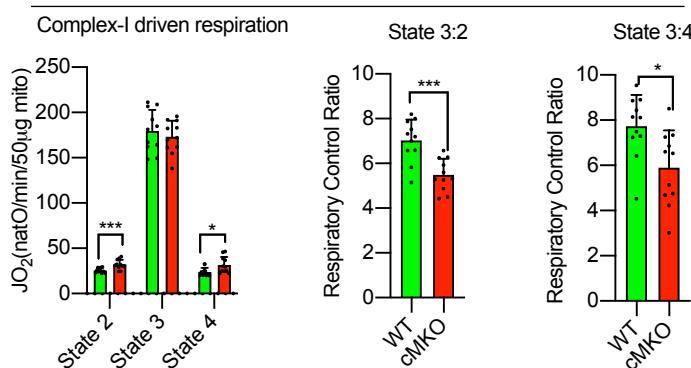
Figure 1

Figure 2

A Primary adult cardiomyocytes

B Mitochondrial content

C
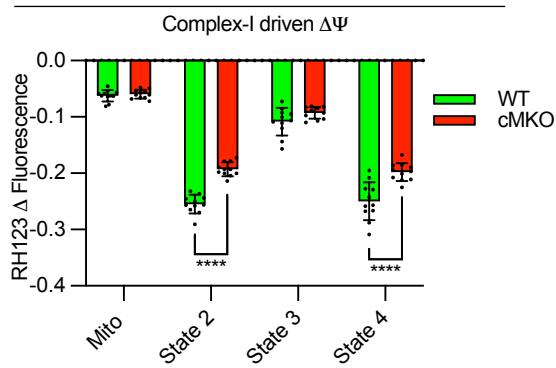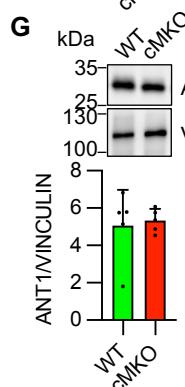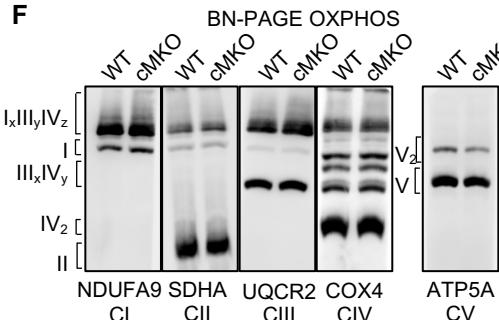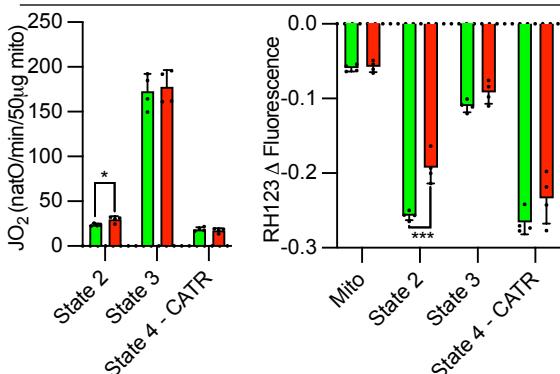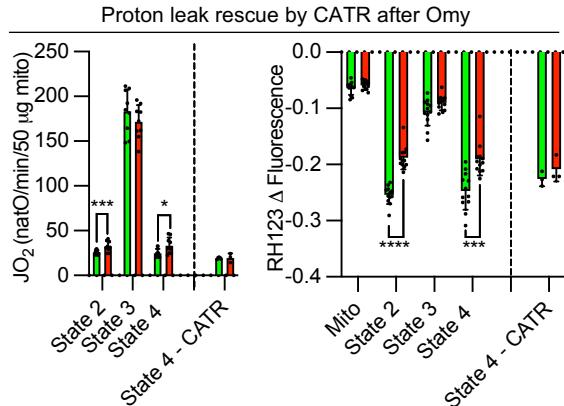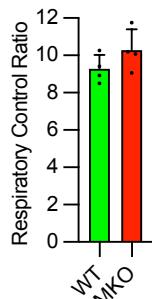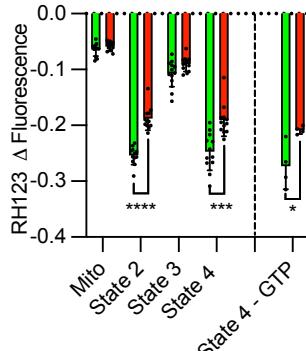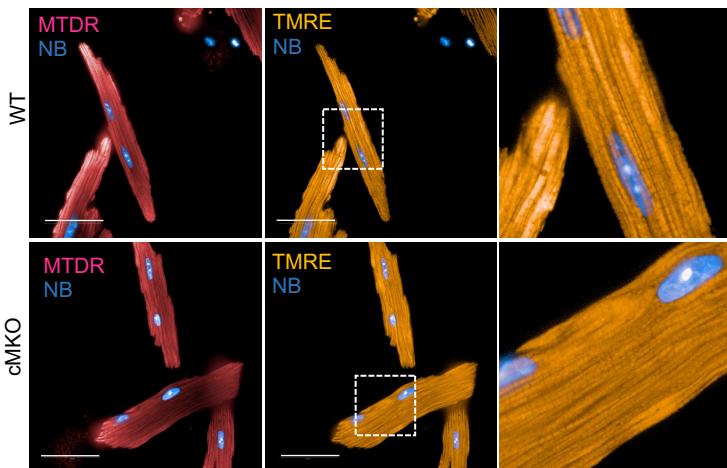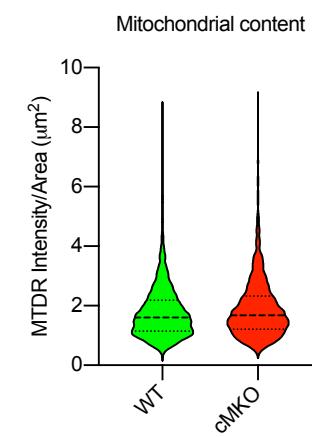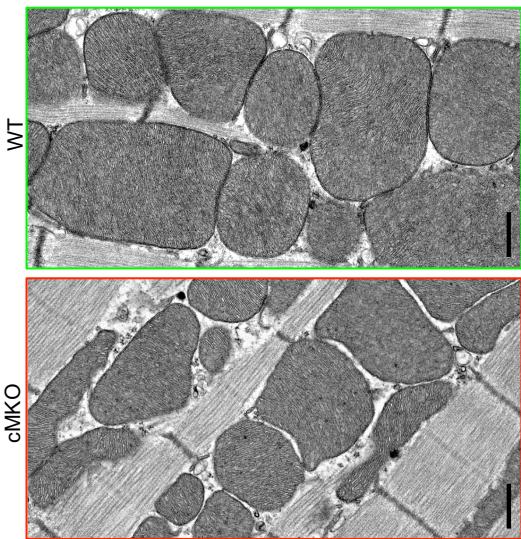
D Mitochondrial area
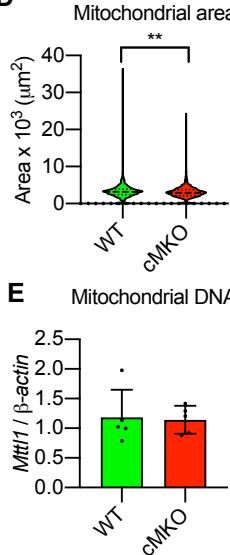
E Mitochondrial DNA
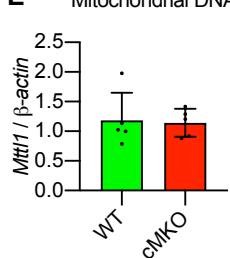
F Cardiac tissue
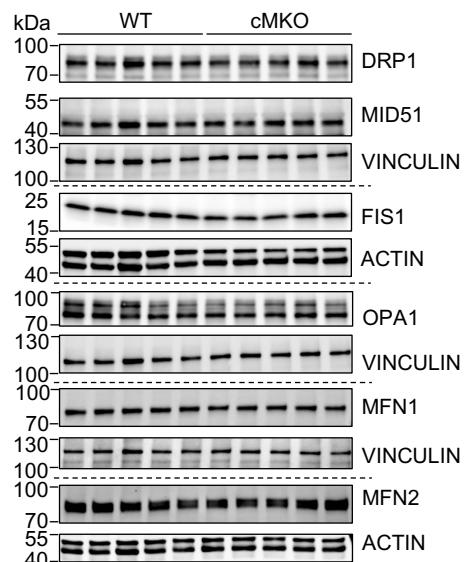
G Stress-induced mitochondrial fission
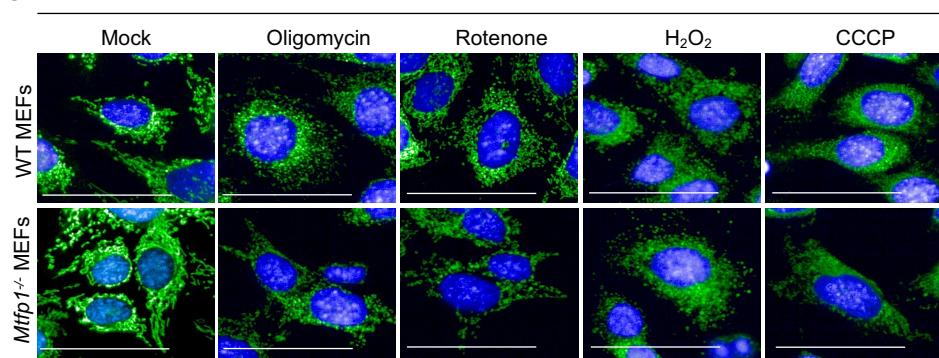
H
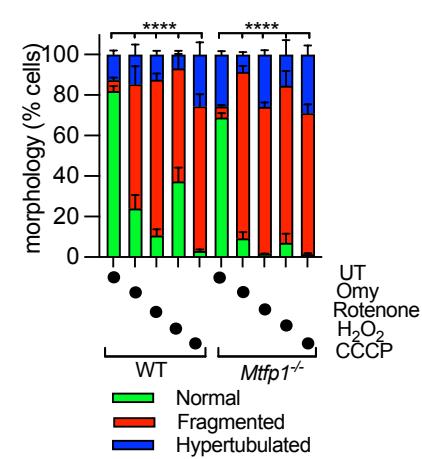
I Mitochondrial morphology in MEFs

J

Figure 3

A Primary Cardiomyocytes – 8 weeks

B CCCP-induced cell death

C Primary Cardiomyocytes – 8 weeks — H₂O₂

D H₂O₂ - induced cell death

E Primary Cardiomyocytes – 8 weeks — Doxorubicin

F Doxorubicin - induced cell death

G Cardiac mitochondria - mPTP opening

H mPTP opening - Maximal swelling

I mPTP opening - MEFs *Ppif⁻/⁻*

Figure 4

J

Actinomycin D + ABT737   + qVD

WT MEFs — NB / PI

Mtfp1⁻/⁻ MEFs — NB / PI

0h   12h   16h   20h   20h

K

PI uptake - ActD + ABT737

- WT
- *Mtfp1⁻/⁻*
- WT qVD
- *Mtfp1⁻/⁻* qVD

cell death (% PI⁺/NucBlue)

Time (h)

L

18h - ActD + ABT737

cell death (% PI⁺/NucBlue)

**** **** ****

WT   *Mtfp1⁻/⁻*   WT qVD   *Mtfp1⁻/⁻* qVD

M

Actinomycin D + ABT737   + qVD

WT MEFs — NB / CE

Mtfp1⁻/⁻ MEFs — NB / CE

0h   6h   12h   14h   14h

N

CE uptake - ActD + ABT737

- WT
- *Mtfp1⁻/⁻*
- WT qVD
- *Mtfp1⁻/⁻ qVD*

Caspase 3/7 activation (% CE⁺/NucBlue)

Time (h)

O

12h - ActD + ABT737

Caspase 3/7 activation (% CE⁺/NucBlue)

**** **** ****

WT   *Mtfp1⁻/⁻*   WT qVD   *Mtfp1⁻/⁻ qVD*

P

Doxorubicin   + qVD

WT MEFs — NB / CE

Mtfp1⁻/⁻ MEFs — NB / CE

0h   6h   12h   16h   16h

Q

CE uptake - Doxorubicin

- WT
- *Mtfp1⁻/⁻*
- WT qVD
- *Mtfp1⁻/⁻* qVD

Caspase 3/7 activation (% CE⁺/NucBlue)

Time (h)

R

16h - Doxorubicin

Caspase 3/7 activation (% CE⁺/NucBlue)

**** **** ****

WT   *Mtfp1⁻/⁻*   WT qVD   *Mtfp1⁻/⁻* qVD

Figure 4 cont

Figure 5

Presymptomatic

Dilated
Cardiomyopathy
18 weeks

Heart
Failure
34 weeks

Middle-aged
death

Birth

Cardiomyocyte KO

Normal structure
& function

Reduced EF

Reduced EF
LV dilatation

Heart Failure
Pulmonary Eodema

Mtfp1

Deletion

↑Cell Death Sensitivity
↑mPTP Opening
↑Mito Uncoupling

↑Cardiac cell death
↑Sterile Inflammation
↓OXPHOS gene expression
↓Mitochondrial respiration

Figure 6